Edith Cowan University

Research Online

2021

Corrosion behavior and characteristics of passive films of laser powder bed fusion produced Ti-6Al-4V in dynamic Hank's solution

Liang-Yu Chen

Hong-Yue Zhang

Chuanbo Zheng

Hong-Yu Yang

Peng Qin
Edith Cowan University

See next page for additional authors

Authors

Liang-Yu Chen, Hong-Yue Zhang, Chuanbo Zheng, Hong-Yu Yang, Peng Qin, Cuihua Zhao, Sheng Lu, Shun-Xing Liang, Linjiang Chai, and Lai-Chang Zhang

materials DESIGN

materials today

Corrosion behavior and characteristics of passive films of laser powder bed fusion produced Ti–6Al–4V in dynamic Hank's solution

Check for updates

Liang-Yu Chen [a,*], Hong-Yue Zhang [a], Chuanbo Zheng [a,*], Hong-Yu Yang [a], Peng Qin [b], Cuihua Zhao [c], Sheng Lu [a], Shun-Xing Liang [b], Linjiang Chai [d], Lai-Chang Zhang [b,*]

[a] School of Materials Science and Engineering, Jiangsu University of Science and Technology, Zhenjiang, Jiangsu 212003, China
[b] School of Engineering, Edith Cowan University, 270 Joondalup Drive, Joondalup, Perth, WA 6027, Australia
[c] Guangxi Key Laboratory of Processing for Non-ferrous Metals and Featured Materials, Guangxi University, Nanning 530004, China
[d] College of Materials Science and Engineering, Chongqing University of Technology, Chongqing 400054, China

HIGHLIGHTS

- Corrosion behavior of laser powder bed fusion produced Ti–6Al–4V samples was investigated.
- Static and dynamic Hank's solutions were selected as the corrosion environments.
- Flow solution degrades passive film of sample and thereby the corrosion resistance.
- Flow solution promotes the deposition of calcium phosphate and hydroxyapatite.

GRAPHICAL ABSTRACT
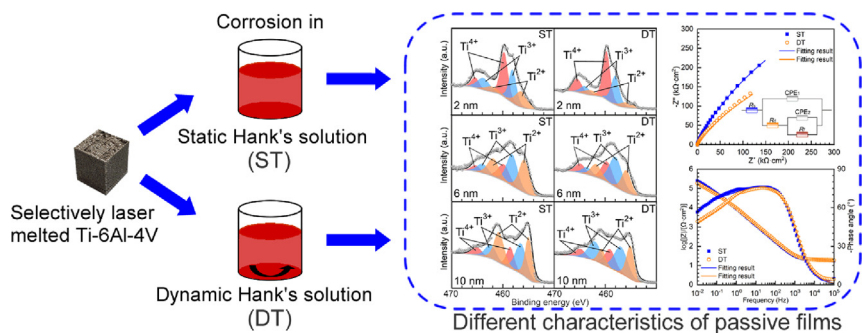
ARTICLE INFO

ABSTRACT

The corrosion behavior of laser powder bed fusion produced (L-PBF-produced) titanium alloys involving flowing body fluid is still unclear. Therefore, this work investigates in vitro corrosion behavior and the characteristics of passive films formed on L-PBF-produced Ti–6Al–4V in both static and dynamic Hank's solutions. Electrochemical measurements, immersion tests, X-ray photoelectron spectroscopy and scanning electron microscopy were conducted. In comparison to the L-PBF-produced Ti–6Al–4V in static Hank's solution, the samples showed lower charge transfer resistance and higher passivation current density (anodic current density as well) in dynamic Hank's solution. Meanwhile, a more apparent deposition of apatite and hydroxyapatite is found on the L-PBF-produced Ti–6Al–4V in dynamic Hank's solution. Such outcomes mainly result from the enhancement of film/solution interfacial transportation in dynamic Hank's solution. The dynamic Hank's solution provides more calcium and phosphate ions to the surface of the passive film and also takes away the dissolved metal ions. Therefore, more salt deposition and a lower-quality passive film are found.

1. Introduction

Additive manufacturing (AM) techniques provide fast ways to produce metallic parts by a layer-wise method from computer-aided design (CAD) models [1–4]. As one of the most common metallic AM techniques, laser powder bed fusion (L-PBF) uses a

* Corresponding authors.
E-mail addresses: lychen@just.edu.cn (L.-Y. Chen), 15952802516@139.com (C. Zheng), lczhangimr@gmail.com, l.zhang@ecu.edu.au (L.-C. Zhang).

laser beam as the heat source to selectively melt metallic powder at a controlled speed under a protective atmosphere [5–8]. By L-PBF, metallic components with near full relative density can be produced. In the last decades, a variety of alloys, such as Ti alloys, steels, Al alloys and Ni alloys, were successfully produced by L-PBF, and the produced alloys were reported to exhibit comparable or even better mechanical properties compared with their counterparts produced by conventional technologies [9–15]. For instance, the laser powder bed fusion produced (L-PBF-produced) Ti–24Sn–4Zr–8Sn exhibits ultimate tensile strength (σ_{UTS}) of 665 MPa with large elongation of 14%, which is slightly better than the forged counterpart with the σ_{UTS} and elongation of 570 MPa and 13% [9,10]. The L-PBF-produced Ti–6Al–4V has higher σ_{UTS} of 1267 MPa and fracture strain of 7.3% than the cast counterpart (σ_{UTS} of 976 MPa and fracture strain of 5.1%) [11–13]. Hot isostatic pressing can close or heal the pores and lack-of-fusion defects of L-PBF-produced Ti–6Al–4V alloy, thereby further enhancing its tensile ductility by about 10% [14,15]. As such, L-PBF-produced Ti and Ti alloys have received considerable attention.

On the other hand, for long-term applications as structural materials, corrosion resistance is also of importance since the metallic components may serve in various aggressive environments. Taking the L-PBF-produced Ti and Ti alloys as examples, considerable endeavors have been made to investigate their corrosion behavior. It was widely reported that the L-PBF-produced Ti–6Al–4V displays significantly different microstructures from that of commercial-grade 5 alloy [6,16–19]. L-PBF-produced Ti–6Al–4V displays dominant acicular α' martensite in its microstructure, while commercial-grade 5 alloy shows a ($\alpha + \beta$) dual-phase microstructure [16]. The acicular α' martensite is considered to be non-equilibrium and in a "higher energy state" concerning corrosion. Therefore, L-PBF-produced Ti–6Al–4V demonstrates inferior corrosion resistance compared with commercial-grade 5 alloy in 3.5 wt% NaCl solution [16]. Zhang et al. [18] and Hamza et al. [19] also found L-PBF-produced Ti–6Al–4V has worse corrosion resistance than a wrought counterpart in the artificial saliva with different fluoride concentrations (0.0020–0.10 M) and pH values (pH = 2–6). Seo et al. [20] used microdroplet cell to investigate the corrosion behavior of acicular α' martensitic grains and prior β grains in the L-PBF-produced Ti–6Al–4V and found that the passive film formed on α' martensitic grains exhibits lower corrosion resistance and is also prone to produce pits. Notably, the volume fractions of α' (or α) and β phases in Ti–6Al–4V alloys influence their corrosion resistance. Dai et al. [21] found that there exists more β phase in the growth plane (i.e. along the build direction) than in the build plane, thereby demonstrating better corrosion resistance in 1 M HCl. The distinction in the corrosion resistance of additively manufactured Ti–6Al–4V resulted from the different volume fractions of α' (or α) and β phases were also reported by other groups [22,23]. The corrosion behavior has also been investigated in other L-PBF-produced Ti alloys, such as Ti–24Nb–4Zr–8Sn [24], Ti–13Nb–13Zr [25], commercial pure Ti (CP–Ti) [26], Ti–TiN and Ti–TiB composites [26]. The aforementioned literature gives a comprehensive evaluation of the corrosion behavior of L-PBF-produced Ti and Ti alloys. Notably, the good corrosion resistance of Ti and Ti alloys is derived from the compact oxide film (passive film) on their surfaces.

Ti and Ti alloys have been used as orthopedic implants for a very long period [27–33]. In the human body, the passive film would be naturally formed on the alloy surface [28–30]. The characteristics of passive films are pertinent to the corrosion behavior of Ti and Ti alloys [22,34,35]. Therefore, lots of works are dedicated to understanding the corrosion behavior of Ti and Ti alloys in the view of the formed passive films. For example, Gai et al. [34] found that the passive film formed on the electron beam melted Ti–6Al–4V has a lower flux of oxygen vacancy than that on the wrought

one in simulated body fluid. Yang et al. [17] reported that the passive film formed on the heat-treated L-PBF-produced Ti–6Al–4V has a relatively higher impedance in 3.5% NaCl solution and hence the alloy has better corrosion resistance. Wang et al. [36] investigated the re-passivation of passive films and successfully illustrated the difference in the pitting corrosion resistance of commercially pure Ti (CP–Ti), Ti–6Al–4V, Ti–29Nb–13Ta–4.5Zr, Ti–35Nb–15Zr, and Ti–25Nb–8Zr. It should be noted that such reported corrosion investigations in literature so far on additively manufactured Ti alloys (as well as other metals) were substantially conducted in static solutions. However, the actual corrosive environments in applications are involving dynamic environments. It is believed that the corrosion behavior of Ti and Ti alloys as well as the formed passive films is different in static and dynamic environments. Chen et al. [27] respectively investigated the solid and porous CP–Ti samples in a dynamic 0.9 wt% NaCl solution with a significantly low rate (2 mL solution pouring per minute from 100 mL solution stored in the storage tank) at 37 °C and their results showed that the passive films formed on both solid and porous CP–Ti samples in dynamic solution have lower charge transfer resistance. However, related works are significantly limited. Especially for laser powder bed fusion technologies, the produced Ti and Ti alloys are widely used for biomedical purposes. Therefore, open questions are raised: how about the distinctions in the corrosion behavior of laser powder bed fusion produced Ti and Ti alloys in static and dynamic simulated body fluid? How about the characteristics of formed passive films? For further applications of laser powder bed fusion produced Ti and Ti alloys, it is of significant importance to answer the questions above.

In this work, L-PBF-produced Ti–6Al–4V was selected as an experimental target since Ti–6Al–4V alloys had been used as knees, hips and elbows, and shoulders [31,37]. Such tissues are always involving flowing body fluid. Therefore, Hank's solution was selected as the electrolyte. To clarify the effect of dynamic Hank's solution on the corrosion behavior of the samples and the characteristics of formed passive films, electrochemical measurements and 30-day immersion tests were conducted. Surface characterizations, such as X-ray photoelectron spectroscopy and scanning electron microscopy, were used to examine the morphologies of passive films and salt deposits. Furthermore, the mechanism for the corrosion behavior of L-PBF-produced Ti–6Al–4V and the formation of the passive film in the dynamic Hank's solution were discussed.

2. Experimental

2.1. Sample and solution preparation

Ti–6Al–4V blocks with dimensions of 10 mm × 10 mm × 10 mm were produced using an MTT SLM 250 HL machine in this work. The powder feedstock was gas-atomized from a Grade 5 Ti–6Al–4V ingot, which had a distribution of D_{10} = 26.9 μm, D_{50} = 39.5 μm, and D_{90} = 48.7 μm. The L-PBF process was conducted in a high purity Ar atmosphere to protect the samples from oxidation. The L-PBF processing parameters used were as follows: the laser power of 200 W, the spot size of 80 μm, the laser scan speed of 1000 mm/s, the layer thickness of 50 μm, and the hatch spacing of 100 μm. Scanning was rotated by 90° between successive layers. The relative density of produced Ti–6Al–4V blocks, examined by the Archimedes method, exceeded 99%. All samples used in this work were as-fabricated and no post-processing was not applied to the samples. The samples for electrochemical measurements and immersion tests were sealed with epoxy resin and then ground and polished to a mirror surface. The edges of electrochemical samples (as well as the samples for

immersion test) were sealed with silicone glue to prevent crevice corrosion. Hank's solution produced by Hank's balanced salts (Heart Biological Technology Co. LTD., China) with the addition of 0.35 g/L $NaHCO_3$ was used as the electrolyte and the main compositions of Hank's solution are 0.140 $g·L^{-1}$ $CaCl_2$, 0.098 $g·L^{-1}$ $MgSO_4$, 0.4 $g·L^{-1}$ KCl, 0.06 $g·L^{-1}$ KH_2PO_4, 8 $g·L^{-1}$ NaCl, 0.048 $g·L^{-1}$ Na_2HPO_4, 1 $g·L^{-1}$ $C_6H_{12}O_6$, 0.35 g/L $NaHCO_3$ and 0.011 $g·L^{-1}$ $C_{19}H_{14}O_5SNa$. The pH of Hank's solution was adjusted to 7.35 by the diluted HCl and NaOH. The Hank's solution was maintained at 37 ± 0.5 °C for electrochemical measurements or immersion tests. The used solutions were prepared with distilled water and analytical grade reagents.

2.2. Microstructural characterizations

An X-ray diffraction (XRD) diffractometer (Empyrean, PANalytical) with Co-K_α radiation was used to analyze the phase constituents of L-PBF-produced Ti–6Al–4V. The scanning range was between 35° and 100° and the scanning rate was 0.03°/s. The software Jade 6.5 was used to analyze the XRD data. An optical microscope (OM, Axioskop2-MAT, Zeiss) was used to characterize the microstructure of the etched alloy sample. The sample for OM microstructure observation was prepared by a standard metallographic procedure and etched in a Kroll reagent (H_2O: HNO_3: HF = 93: 5: 2, in vol%). A JEM-2100F transmission electron microscope (TEM, JEOL Ltd., Japan) operated at 200 kV was used for TEM characterizations. The samples for TEM characterizations were ground to about 100 μm thick and then were thinned by a twin-jet polishing machine with a mixed solution composed of $HClO_4$: C_4H_9OH: CH_3OH = 1: 3: 6 (in vol%) at the temperature of minus 30 °C. A scanning electron microscope (SEM, Supra 55, Zeiss) equipped with an energy dispersive X-ray spectroscopy (EDS) detector with an acceleration voltage of 5 kV was used to characterize the morphologies of the samples after potentiodynamic polarization tests and 30-day immersion tests in secondary electron mode. The EDS results are obtained from K radiation (including K_α and K_β radiation).

2.3. Electrochemical measurements

An electrochemical workstation with a three-electrode system (CHI660E, Chenhua) was used to examine the electrochemical performance of samples in this work. In this system, the L-PBF-produced Ti–6Al–4V was used as the working electrode, a platinum sheet was used as the counter electrode and a saturated calomel electrode (SCE) was used as the reference electrode. The exposure area of the sample used for electrochemical measurements was about 1.0 cm^2. Open circuit potential (OCP) was measured and recorded for 1800 s to ensure the stability of alloy samples in Hank's solution. After OCP measurement, electrochemical impedance spectroscopy (EIS) was conducted potentiostatically, which was run at peak-to-peak sinusoidal voltage signals of 10 mV over the frequency range between 10^{-2} Hz and 10^5 Hz. The EIS data processing was conducted using the software ZsimpWin 3.30. Afterward, potentiodynamic polarization tests were performed with a sweeping range of −0.25 to +2 V (vs. OCP) at a sweeping step of 0.1667 mV/s. The potentiodynamic polarization results were processed by the software Cview 2.6. The potentiostatic polarization was employed to generate the passive film on the L-PBF-produced Ti–6Al–4V. Based on the passivation region derived from potentiodynamic polarization curves, 0.6 V_{SCE}, 0.7 V_{SCE}, 0.8 V_{SCE}, 0.9 V_{SCE}, and 1.0 V_{SCE} were selected as the applied potentials in the potentiostatic polarization treatments. EIS measurements were subsequently conducted at each potentiostatic potential. The acquired data were also processed by ZsimpWin software. The capacitance vs. frequency curve of the tested sam-

ples could be obtained. The capacitance at 1 kHz was selected as effective capacitance [38], which was used to calculate the thickness of the passive film. Afterward, Mott-Schottky measurements were conducted at the frequency of 1 kHz, sweeping the potential from + 0.8 V (vs. OCP) to −0.8 V (vs. OCP) with a step of 10 mV/s. Note that, all the potentials reported in this work were reported against SCE. Each electrochemical test was repeated at least three times for data reproducibility.

It should also be noted that all electrochemical tests were carried out in a beaker containing 800 mL Hank's solution, respectively. Hank's solution was achieved using a Teflon cylinder magnetic stirrer in the beaker. The stirrer used was in the dimensions of 30 mm long and 8 mm diameter. During the electrochemical measurements, the stirrer was set to 20 rpm to keep the electrolyte flowing because of the following consideration. If selecting a significantly low flowing rate of electrolyte, the results may be not apparent; however, in laboratory conditions, the flowing rate over 20 rpm would result in the overflow of electrolyte in the beaker and the instability of electrochemical measurements. Therefore, a flowing rate of 20 rpm was selected to obtain relatively evident and stable results. Hereafter, the Ti–6Al–4V alloys tested in the static solution were denoted as ST, while those tested in the dynamic solution were denoted as DT. Due to the anisotropy of L-PBF-produced metals [21], the plane of sample contacting solution is the building plane (i.e. the X-Y plane) in all examinations including microstructural characterizations, electrochemical measurements and immersion tests.

2.4. Immersion tests

Immersion tests were also carried out in the static and dynamic Hank's solutions with the same parameters, respectively. In comparison to electrochemical measurements, the sample surfaces were placed toward the outside of the beaker to obtain a more evident result since the flowing rate of the electrolyte increased with increasing the distance to the center of the beaker under such a condition. To avoid the evaporation of electrolytes, the beaker was covered by plastic wrap during the immersion tests. Three individual samples as a group in parallel were immersed in a beaker and the immersion tests were executed for 30 days. After the immersion test, some immersed samples were further used for EIS measurements in the static Hank's solution. Meanwhile, the concentrations of Ti, Al, and V ions contained in the electrolytes after the immersion tests were analyzed by inductively coupled plasma atomic emission spectroscopy (ICP-AES, 7700x, Agilent).

## 2.5. X-ray photoelectron spectroscopy characterization

The immersed samples were analyzed by X-ray photoelectron spectroscopy (XPS, ESCALAB 250XI, Thermofischer) to investigate the composition data in depth. Al K_α X-ray was performed as the source (hv = 1486.6 eV) at 15 kV and 10 mA. The diameter of the spot was about 500 μm. During the test, the surfaces of immersed samples were etched with Ar ions (etching rate was about 0.2 nm/s). The XPS spectra were calibrated according to C1s standard peak (with the binding energy of 284.6 eV). The software Thermo Avantage 5.979 was used to fit the peaks in the XPS spectra, using Shirley mode as the background.

3. Results

3.1. Microstructural features

Fig. 1 shows the XRD pattern and microstructural images of L-PBF-produced Ti–6Al–4V. As shown in Fig. 1a, only α′ phase is
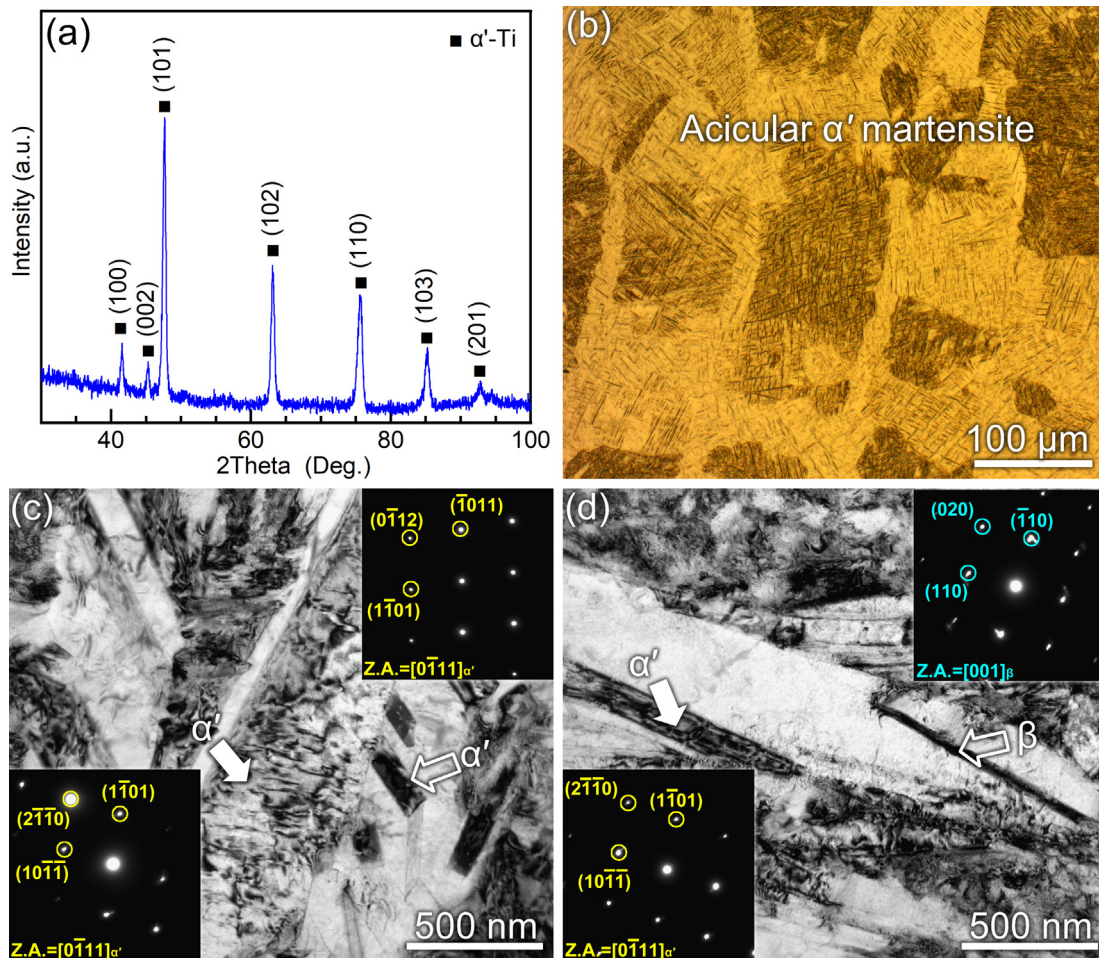
Fig. 1. Microstructural features of selective laser melted Ti–6Al–4V used in this work: (a) XRD pattern, (b) optical image, (c) and (d) TEM images at two random locations. The insets in (c) and (d) are the selected area diffraction patterns for specific phases.

observed on the XRD pattern. Although Ti–6Al–4V is a dual-phase alloy, no peaks of β phase are found. This finding indicates a very low volume fraction of β phase in the microstructure. Similar outcomes were also reported in the literature, e.g., Refs. [39–43]. Since the β-stabilizer V has limited diffusion in the melt owing to the fast-cooling rate in the L-PBF process, L-PBF-produced Ti–6Al–4V usually has less β phase than the cast or annealed counterparts [16,17]. A typical acicular α′ martensitic microstructure is observed under OM observation (Fig. 1b). Such a microstructure is also frequently observed in Ti and Ti alloys, which are fast cooled from β region to α region due to the rapid transformation of body-centered cubic structure to hexagonal close-packed structure [6]. To confirm the existence of β phase in the microstructure, TEM examinations were carried out. Fig. 1c and 1d are TEM images for the microstructure of the L-PBF-produced Ti–6Al–4V samples at two random locations, in which many martensite laths with a large number of dislocations are observed. It was reported that β phase is presented between the laths in lath-structured Ti–6Al–4V [39,44]. However, in Fig. 1c, clear lath boundaries are observed and no separated β grains are observed. The grains with different features are characterized as α′ grains (Fig. 1c insets). In Fig. 1d, an α′ grain was characterized near an α′ lath with a relatively large area. A dark rod with a length of ~ 1000 nm and a width of ~ 40 nm is found in this lath, which is characterized as β grain. After a dedicated TEM examination of the microstructure, only a few β grains with such a morphology are observed. Therefore, one can conclude that the L-PBF-produced Ti–6Al–4V has a large amount of acicular
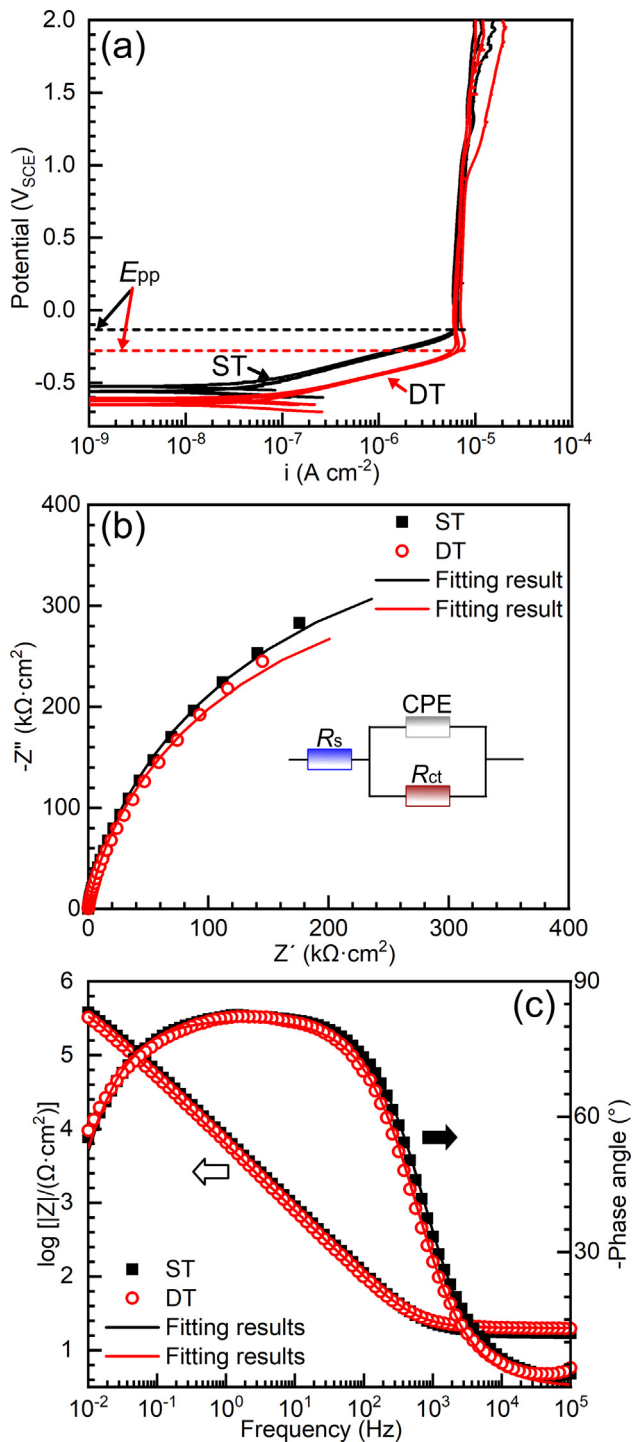
α′ martensite phase and considerably less β phase in the microstructure.

3.2. Electrochemical corrosion behavior

Fig. 2 is the electrochemical results of L-PBF-produced Ti–6Al–4V in both static and dynamic Hank's solutions at 37 °C. As seen in Fig. 2a, the potentiodynamic polarization curves of both alloy samples demonstrate good reproducibility. The fitted results of potentiodynamic polarization curves are listed in Table 1. Under both conditions, the sample displays passivation behavior. The DT sample has a slightly lower corrosion potential (E_{corr}) (-0.627 ± 0.019 V_{SCE}) than the ST counterpart (-0.548 ± 0.016 V_{SCE}). As E_{corr} estimates the energy of corrosion reaction, the result indicates that the DT sample requires lower energy to be oxidized compared to the ST sample. Fitting potentiodynamic polarization curves using the software Cview 2.6, the corrosion current densities (I_{corr}) for both ST and DT samples are 0.008 ± 0.004 μA·cm^{-2} and 0.030 ± 0.003 μA·cm^{-2}, respectively. According to Faraday's law, the corrosion rates of both samples can be expressed as [45]:

$$Corrosion\ rate = \frac{MI_{corr}}{nF\rho_m} \qquad (1)$$

where corrosion rate is in mm/y, M is the molar mass of alloy (47.87 g/mol for Ti), n is the charge of Ti ion, F is the Faraday constant (96,487 C·mol^{-1}), and ρ_m is the density of the alloy (4.43 g/cm^3 for Ti–6Al–4V [46]). For an approximate calculation, the molec-

Fig. 2. Electrochemical results of ST and DT samples in Hank's solution at 37 °C: (a) potentiodynamic polarization curves, (b) Nyquist diagram, (c) Bode diagram. ST and DT indicate the selective laser melted Ti–6Al–4V tested in static and dynamic Hank's solutions at 37 °C, respectively.

ular weight of Ti was used. As calculated, the corrosion rates for ST and DT are 0.071×10^{-3} mm/y and 0.265×10^{-3} mm/y, respectively. The anodic reactions of Ti corresponding to spontaneous passivation in Hank's solution can be simply expressed as [26]:

$$Ti^{4+} + 6Cl^- \rightarrow [TiCl_6]^{2-} \tag{2}$$

$$[TiCl_6]^{2-} + 2H_2O \rightarrow TiO_2 + 6Cl^- + 4H^+ \tag{3}$$
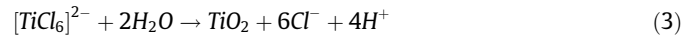
For passive metals, the migration of ions during corrosion is mainly determined by the formed passive films [47]. Therefore, passivation potential (E_{pp}) and passivation current density (I_{pp}) are two key parameters to estimate the corrosion resistance of passivated metals. E_{pp} illustrates the starting point of metallic materials entering the passivation region; in general, the lower the E_{pp}, the easier the material is passivated. I_{pp} demonstrates the migration of ions in the passive film after complete passivation [16]. On the anodic branches of potentiodynamic polarization curves, DT is passivated at the potential of about -0.261 ± 0.014 V$_{SCE}$, while ST is passivated at the potential of about -0.160 ± 0.004 V$_{SCE}$. After completing passivation, the ST sample has the I_{pp} of 6.355 ± 0.167 µA·cm^{-2}, which is slightly lower than that of the DT sample (6.683 $\pm$ 0.526 µA·cm^{-2}). Therefore, L-PBF-produced Ti–6Al–4V is more prone to be corroded in the dynamic Hank's solution.

Fig. 2b and c represents the Nyquist diagrams and Bode diagrams for DT and ST samples. As seen from Fig. 2b, the capacitive loop of ST shows a larger radius compared with that of DT. It is known that the radius of the capacitive loop in the Nyquist diagram illustrates the impedance of the formed passive film on the sample surface; the capacitive loop with a larger radius generally specifies the higher impedance of passive film [48]. Hence, it illustrates that the impedance of passive film formed on ST is slightly higher than that on DT. In Bode impendence diagram, two distinct regions are observed. A flat portion of the curve is found from middle to high frequency (10^3–10^5 Hz), which response to the resistance of electrolyte. In the frequency of 10^{-2}–10^3 Hz, the impendence increases with decreasing the frequency, displaying a linear relationship (Fig. 2c). In the Bode phase angle diagram, the phase angle approaches 0° at high frequency, which also indicates the constant resistance of electrolytes in the EIS measurements [44]. The values of phase angles show the maximum values (over ~75°) and are independent of the frequency for both DT and ST in the range of 10^{-1}–10^2 Hz (Fig. 2c). Such results suggest the non-ideal capacitive behavior of passive films formed on the L-PBF-produced Ti–6Al–4V alloy samples [24]. Although salt deposition may take place when Ti alloys are immersed in Hank's solution [49,50], open circuit potential lasted only 1800s before the EIS tests. Therefore, it is considered that the salt deposition is significantly slight, which would be presented in the following. As such, a typical equivalent electrical circuit model $R(QR)$ (Fig. 2b inset) is used to describe the data obtained, where R_s is solution resistance, R_{ct} indicates charge transfer resistance and CPE is a constant phase element. Due to the complicated corrosion process, capacitor of passive film is not ideal. Therefore, CPE is used to describe the shift from the ideal capacitor. The impedance of CPE can be defined by the following equation [51]:

Table 1
Fitting results of potentiodynamic polarization curves and calculated corrosion rate for laser powder bed fusion produced Ti–6Al–4V in both static (ST) and dynamic (DT) Hank's solutions at 37 °C. E_{corr} is the corrosion potential; I_{corr} is the corrosion current density; E_{pp} is the passivation potential, I_{pp} is the passive current density.

Sample	E_{corr} (V$_{SCE}$)	I_{corr} (µA·cm^{-2})	E_{pp} (V$_{SCE}$)	I_{pp} (µA·cm^{-2})	Corrosion rate (mm/y)
ST	-0.548 ± 0.016	0.008 ± 0.004	-0.160 ± 0.004	6.355 ± 0.167	0.071×10^{-3}
DT	-0.627 ± 0.019	0.030 ± 0.003	-0.261 ± 0.014	6.683 ± 0.526	0.265×10^{-3}

$$Z_{CPE} = \frac{1}{Q(j\omega)^n} \tag{4}$$

where Q is CPE constant, ω is angular frequency (in rad/s), $j^2 = -1$ is imaginary number, and n is CPE exponent. For $n = 0$, CPE is a resistance, whilst CPE behaves as a capacitance for $n = 1$. The fitted results of EIS are listed in Table 2. χ^2 is less than 0.001, indicating a good quality of fitting. R_{ct} indicates the resistance of charge transferring from metal to electrolyte. The R_{ct} for ST (0.774 ± 0.15 MΩ cm^2) is slightly larger than that for DT (0.689 ± 0.11 MΩ cm^2). Therefore, ST displays better corrosion resistance than DT in Hank's solution.

Additionally, SEM images with corresponding EDS spectra for the morphologies of ST and DT samples after potentiodynamic polarization tests are shown in Fig. 3. Before presenting the results, it should be noted that EDS is a semi-quantitative method for the chemical compositions of the analyzed materials. The electron beam penetrates the examined surface at a certain depth (about 1 μm) depending on the accelerated voltage of SEM and the analyzed materials [52]. Meanwhile, due to the size of the beam spot (about 1.5 μm in diameter in this work), the data were collected from a small area but not an exact point [52]. Therefore, the examined region in the L-PBF-produced Ti–6Al–4V material was a cylinder with a diameter of 1.5 μm and a depth of 1 μm. As known, the passive films formed on Ti–6Al–4V alloys are extremely thin, which is only several to dozens of nanometers in thickness [53]. As a result, the obtained EDS results might contain the compositions of the substrate. Hence, the presented EDS results are only a qualitative analysis for the corroded surface but not quantitative results. Three typical morphologies, namely, manufacturing defects (Fig. 3a and d), pits (Fig. 3b and e), and corrosion products (Fig. 3c and f) in both static and dynamic Hank's solution are presented. Unlike the conventional Ti–6Al–4V [54], different phases are hardly distinguished from the surface of the passive film due to the significantly low fraction of β phase. As mentioned in Section 2.1, Hank's solution contains a variety of salts and hence the elements in such salts may be found on the surfaces of corroded samples. Fig. 3a shows the manufacturing defect (pore) on the surface of ST sample. Trace P is found at the corner of pore, indicating the deposition of trace compounds containing P is deposited. Although the detected contents of P are very low, the presence of a small peak confirms the existence of P (Fig. 3a-A). In comparison to the corrosion in NaCl solution, corrosion in Hank's solution could result in salt deposition, caused by preferential adsorption of phosphate ions [49,50,55]. Therefore, it is reasonable to detect P on the surface of the corroded sample. Fig. 3b shows a typical morphology of the pit, which results from the rupture of the passive film [20]. Pitting corrosion of L-PBF-produced Ti alloys was reported by Dai et al. [21] and Seo et al. [20]. The EDS results show that the corrosion products containing Ca and P are accumulated in the pit. It is also found that Al is preferentially dissolved in the pit (Fig. 3b-B). This finding confirms that this is a pit but not a manufacturing defect due to the preferential dissolution. A similar finding was reported in Al–Ti alloys [56]. Meanwhile, in the view of the formation of manufacturing defects in the L-PBF-produced Ti alloys, the defects are always deep and in irregular shape, if it is produced by unmelted particles or imperfect collapse (keyhole)

[6]. Such two aspects differentiate the corrosion pits from manufacturing defects in the L-PBF-produced Ti–6Al–4V. Some corrosion products are also observed on the surface of ST sample (Fig. 3c). Due to the small size of corrosion products (below 1 μm), only trace Ca and P are detected (Fig. 3c-C), indicating that the corrosion products may consist of calcium phosphate, which is consistent with the results in Refs. [49,50]. Similar phenomenon is also observed in the dynamic Hank's solution. By contrast, more P and Ca are found on the surface of corroded DT sample, in all three typical morphologies (Fig. 3d–f). Especially, the size of corrosion products on DT sample reaches several microns (Fig. 3f), which is significantly larger than that on ST sample (Fig. 3c). Such a finding demonstrates salt deposition is prone to take place in the dynamic Hank's solution, even in such a short period.

3.3. Characteristics of passive films formed on samples after potentiostatic polarization

During corrosion, the growth of passive films on metals stems from the migration of ions and point defects [57]. Therefore, to further understand the characteristics of passive films formed on ST and DT, potentiostatic polarization and subsequent Mott-Schottky (M-S) measurements were conducted. Fig. 4 reveals the potentiostatic polarization curves for both ST and DT in the range of 0.6–1 V_{SCE}. The values for the current density in all curves rapidly decrease with increasing time, indicating the formation of passive films. Subsequently, the current density is stabilized. The insets in both Fig. 4a and 4b are the magnified images from 25 min to 30 min. Within this period, the current density decreases at a significantly low rate. The quasi-steady-state current density produced by high applied potential is higher than that produced by low applied potential [34]. After 30-min potentiostatic polarization, the quasi-steady state current density for DT ranges from about 0.03 to 0.08 μA cm^2, which is almost 1.5 times larger than that for ST (about 0.02 to 0.05 μA cm^2). According to Macdonald's model [57], the following equation can be used to fit the growth kinetics of passive film:

$$\log i = \log A + n \log t \tag{5}$$

where i is the current density, t is the polarization time (in second), A and n are constants. When the value n approaches -1, a compact and protective passive film forms [44]. The fitting results of n are -0.73 ± 0.02 and -0.69 ± 0.03 for ST and DT, respectively, elucidating that the passive film formed on ST is relatively compact compared with that formed on DT.

Fig. 5 shows the M-S curves of passive films on ST and DT formed from 0.6 V_{SCE} to 1 V_{SCE}, respectively. A typical linear region with a positive slope in the applied potential of about -0.3 V_{SCE} to -0.5 V_{SCE} indicates that the passive films on ST and DT show typical n-type semiconductive properties. Therefore, electron donors, which are in the form of oxygen vacancies, exist in the passive film [58]. The density of the donor (N_D) is calculated to better understand the semiconductive properties of passive films, which can be derived from the following equation [58]:

$$C^{-2} = C_{sc}^{-2} = \frac{2}{\varepsilon\varepsilon_0 e N_D}\left(E - E_{FB} - \frac{kT}{e}\right) \tag{6}$$

Table 2
Fitting results of electrochemical impedance spectra for laser powder bed fusion produced Ti–6Al–4V in both static (ST) and dynamic (DT). R_s means solution resistance, R_{ct} indicates charge transfer resistance, CPE describes charge transfer capacitance, n is the exponents of CPE, and χ^2 is the sum of squares of the differences between theoretical and experimental points.

Sample	R_s (Ω·cm^2)	CPE × 10^{-5} (F·cm^{-2})	n	R_{ct} (MΩ·cm^2)	χ^2
ST	17.30 ± 0.79	2.58 ± 0.75	0.9127 ± 0.0191	0.774 ± 0.15	5.29 × 10^{-4}
DT	20.03 ± 0.72	2.98 ± 0.82	0.9083 ± 0.0185	0.689 ± 0.11	8.82 × 10^{-4}
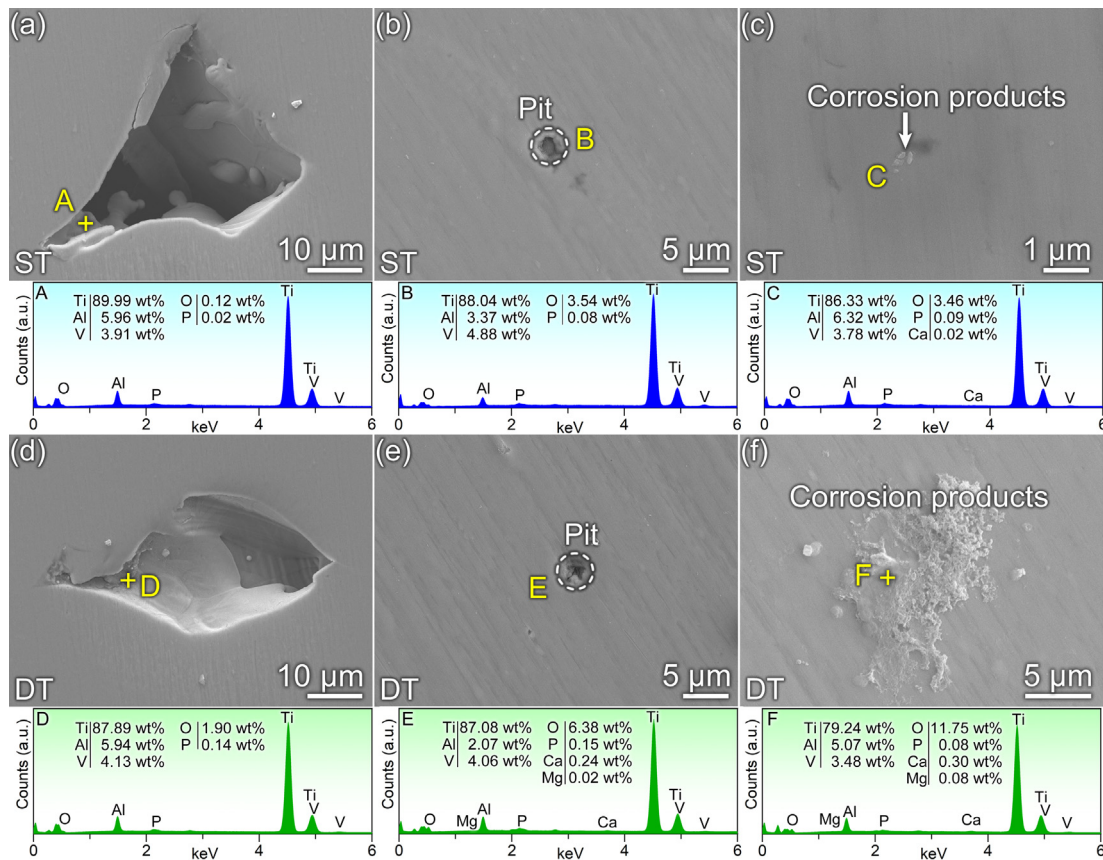
Fig. 3. Secondary electron SEM images of surface morphologies of the selective laser melted Ti–6Al–4V samples after potentiodynamic polarization tests: (a), (d) manufacturing defect, (b), (e) pits and (c), (f) corrosion products on the surfaces of ST and DT samples. The corresponding EDS spectra are below the SEM images. ST and DT indicate the selective laser melted Ti–6Al–4V tested in static and dynamic Hank's solutions at 37 °C, respectively.

where C_{sc} is the space charge capacitance; ε is the relative dielectric constant of the passive film (considering the main phase constituent of TiO_2 in the passive film; ε is taken as 60 in this work [34]); ε_0 is the vacuum dielectric constant (8.85×10^{-14} F·cm^{-1}); e is the electronic charge (1.60×10^{-19} C); k is the Boltzmann constant (1.38×10^{-23} J·K^{-1}); T is the absolute temperature; E is the film formation potential; E_{FB} is the flat band potential. $\frac{kT}{e}$ is significantly small at room temperature, hence it can be neglected. Therefore, in terms of Eq. (6), C^{-2} is inversely proportional to N_D. Fig. 6a displays the changes in N_D as a function of applied potential. Apparently, N_D declines with increasing the applied potential for both samples, specifying the reduction in the conductivity of passive films. The passive film of ST reveals lower N_D, indicating better protectiveness in Hank's solution.

Meanwhile, the thickness of the formed passive film (L_{SS}) can be calculated by the following equation [34]:

$$L_{SS} = \frac{\varepsilon \varepsilon_0 A}{C_{eff}} \tag{7}$$

where A is the effective passivation area of Ti electrode, C_{eff} is the effective capacitance that can be derived from EIS data. In general, the electrochemical impedance exhibits a nearly pure capacitive behavior above the frequency of 1 kHz [59]. As such, the thicknesses of passive films formed on ST and DT samples can be obtained, which is plotted in Fig. 6b. At the same applied potential, the passive film formed on DT samples is slightly thicker. Meanwhile, the diffusion coefficient of oxygen vacancies can be deduced based on the calculated N_D. It was also reported that the relationship between N_D and film formation potential can be written as [38]:

$$N_D = \omega_1 e^{(-bE)} + \omega_2 \tag{8}$$

where ω_1, ω_2 and b are fitted constants using Eq. (8). The values of ω_2 for ST and DT are shown in Fig. 6a, which are 1.97×10^{19} and 1.96×10^{19}, respectively. According to the Nernst-Plank transport equation [60], $\omega_2 = \frac{i_p RT}{4eF\varepsilon D_o}$; therefore,

$$D_o = \frac{i_p RT}{4eF\varepsilon_L \omega_2} \tag{9}$$

where i_p is the quasi-steady-state current density, which could be derived from Fig. 4, R is gas constant (8.314 J·mol^{-1}), and ε_L is the electric field intensity in the formed passive film, which can be calculated from the relationship between L_{SS} and E, illustrating as the Eq. (10):

$$L_{SS} = \frac{(1-\alpha)E}{\varepsilon_L} + B \tag{10}$$

where α is the polarizability of the passive film/solution interface (taking the $\alpha = 0.5$ [34]) and B is a constant. The calculated ε_L for ST and DT are 1.47×10^7 V/m and 1.00×10^7 V/m, respectively. Therefore, D_o for the passive films formed on ST and DT can be estimated, which is plotted in Fig. 6c. Apparently, the passive film formed on Ti–6Al–4V in the dynamic Hank's solution has a higher D_o. Based on these results, one can conclude that the passive film formed on DT has a higher growth rate. Although the passive films formed on DT are thicker (Fig. 6b), the DT still has higher quasi-steady-state current densities than the ST at the given potentials, illustrating that the dynamic Hank's solution degrades the quality of the formed passive film on L-PBF-produced Ti–6Al–4V.
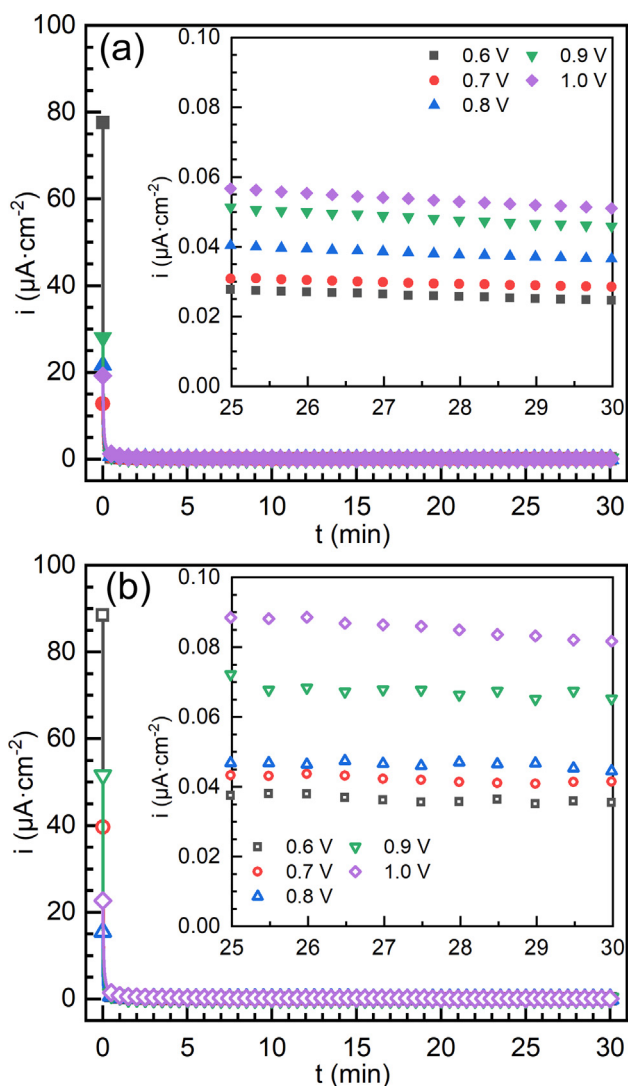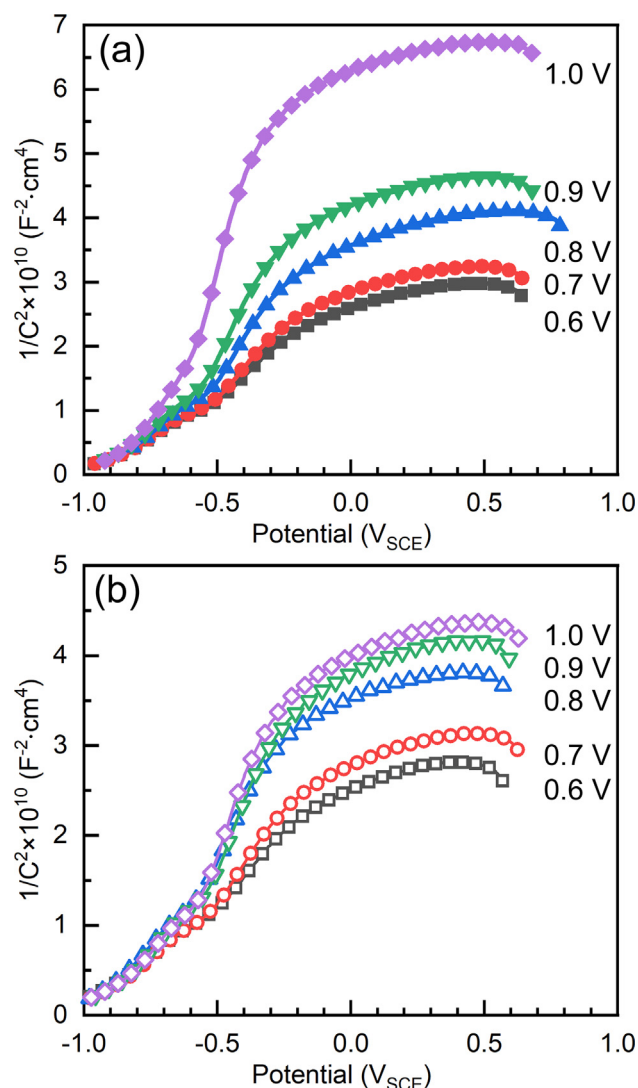
Fig. 4. Anodic polarization curves from 0.6 to 1 V_{SCE}: (a) ST and (b) DT. The insets are the magnified images from 25 min to 30 min. ST and DT indicate the selective laser melted Ti–6Al–4V tested in static and dynamic Hank's solutions at 37 °C, respectively.

Fig. 5. Mott-Schottky behavior of passive films formed on (a) ST and (b) DT at 0.6–1 V_{SCE}. ST and DT indicate the selective laser melted Ti–6Al–4V tested in static and dynamic Hank's solutions at 37 °C, respectively.

3.4. 30-day immersion test

All tests conducted above specify the corrosion resistance of L-PBF-produced Ti–6Al–4V in both static and dynamic Hank's solutions and the characteristics of formed passive films in a short term. However, for corrosion-resistant materials, long-term performance is a critical consideration for their lifetime in service environments [61]. Therefore, 30-day immersion tests for L-PBF-produced Ti–6Al–4V in both static and dynamic Hank's solutions were conducted. In such a case, passive films are spontaneously formed on sample surfaces but not driven by the electric field.
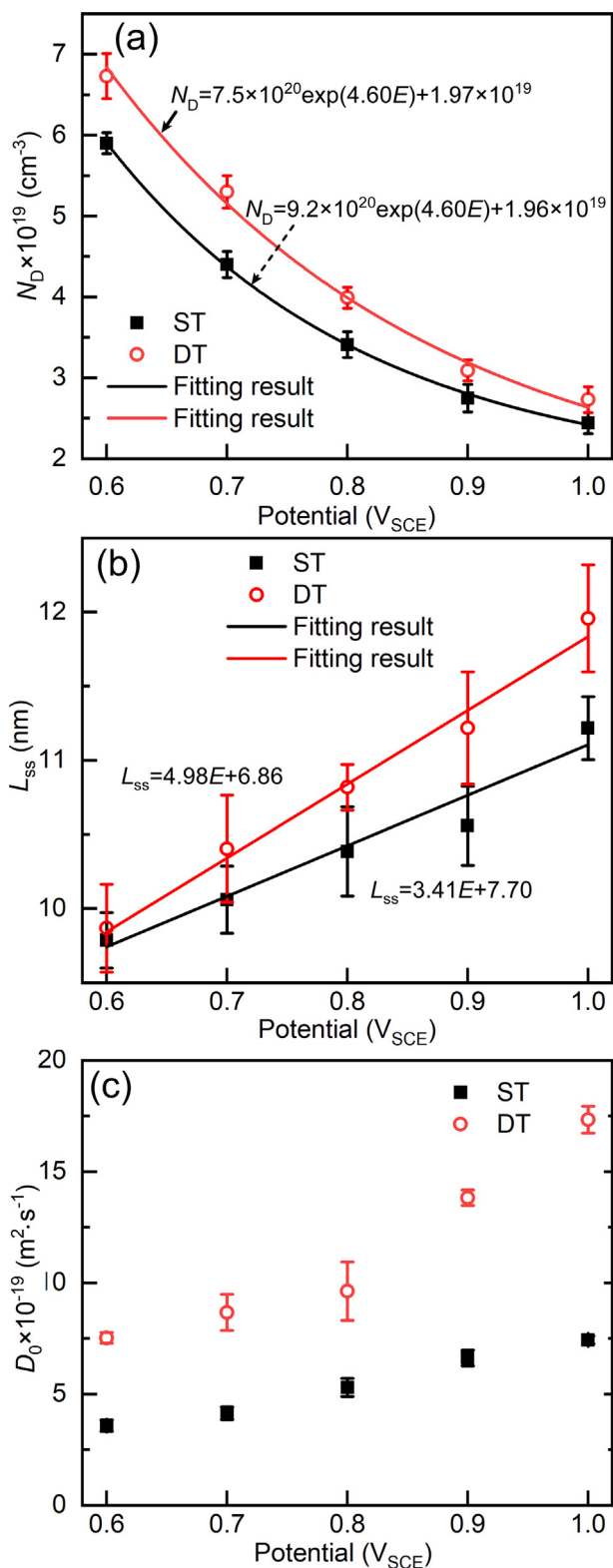
3.4.1. Ions release and surface morphologies

The ion release is an important consideration for the applications of Ti and Ti alloys, especially for biomedical use [49]. The concentrations of Ti, Al, and V ions in Hank's solution after 30-day immersion tests were examined by ICP-AES (Fig. 7). This value is the sum of ion release from three samples with a total surface area of 3 cm² after 30-day immersion. The concentration of Ti ion released by ST is only 0.0011 mg/L. In comparison, the DT sample releases significantly more Ti ions (0.0363 mg/L). Similarly, ST

releases less Al ion (0.0363 mg/L) than DT (0.0516 mg/L). A wide range of diseases may be triggered by taking excessive Al ions, including Alzheimer's disease and osteoporosis [62]. In this work, the volume of Hank's solution is 0.8 L and hence the total content of ion release is lower than 1 mg after a 30-day immersion test. The upper limit of daily intake for humans is evaluated to be 1 mg/kg of body weight [62]. For a simple calculation, the weight of an adult male is estimated to be 70 kg, indicating that a patient with implants cannot intake more than 70 mg Al ions daily. This amount includes the ion release from implants and daily intake from food and water. Although the exposure surface of the sample is only 1 cm², the ion release would not exceed the upper intake for the human body when using a Ti implant (at most hundreds of square centimeter surface). The concentration of V is extremely low in both static and dynamic Hank's solutions, even lower than 0.001 mg/L (lower than the accuracy of the instrument). These results can be illustrated by the Ellingham-Richardson theory [34]. In a large range temperature, the Gibbs free energy needed for the oxidation of elements is Al < Ti < V. Therefore, Al is most likely to be oxidized during corrosion. On the other hand, Al ions are always associated with oxygen vacancies in the oxide formed on Ti and Ti alloys to keep local electroneutrality [63]. Therefore,

Fig. 6. Calculated semiconductive properties of passive films formed on ST and DT after anodic polarization at 0.6–1 V_{SCE}: (a) donor densities, (b) thicknesses and (c) diffusion coefficients of oxygen vacancy. ST and DT indicate the selective laser melted Ti–6Al–4V tested in static and dynamic Hank's solutions at 37 °C, respectively.
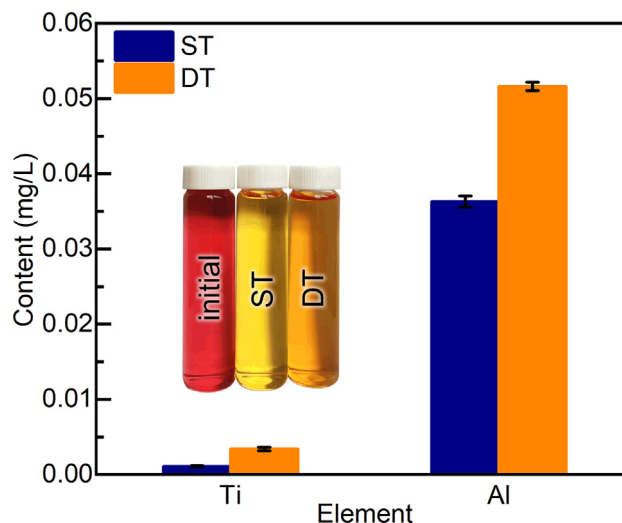
Fig. 7. Contents of Ti and Al ions in Hank's solution after a 30-day immersion test: (a) ST and (b) DT. Inset shows Hank's solution before and after the test under different conditions. ST and DT indicate the selective laser melted Ti–6Al–4V tested in static and dynamic Hank's solutions at 37 °C, respectively.

flat surfaces, 30-day immersed samples show somewhat different and complicated corroded surfaces due to the salt deposition. Fig. 8 shows some characteristic morphologies on both samples. Fig. 8a shows the manufacturing defect (irregular-shaped pore) on the surface of the ST sample, resulted from an unmelted particle. Only trace P is detected in the pore (Fig. 8-A), which is similar to the finding in the manufacturing defect of the sample after the potentiodynamic polarization test. However, salt deposition becomes apparent on the surface of the 30-day immersed ST sample. Fig. 8b shows a balling (another type of manufacturing defect) on the surface of the ST sample. No cracks, pits, and large-sized corrosion products are found. Trace P, Ca and about 2 wt% O are detected at location B beside the compositions of the substrate (Fig. 8-B). It was reported that calcium phosphate could be naturally formed on the surface of Ti and Ti alloys in Hank's solution at 37 °C [49]. Fig. 8c reveals the features of the general surface with no manufacturing defects and large-sized corrosion products. The EDS result (Fig. 8c-C) is approximate to that in Fig. 8b, further confirming that salt deposition takes place after 30-day immersion. A small corrosion product with a size of ~1 μm is found in Fig. 8d. As seen in Fig. 8d inset, the corrosion products are assembled in a small manufacturing defect. A considerable amount of P and Ca are found in the corrosion products (Fig. 8d-D), which are the deposited calcium phosphates as described in Ref. [50]. In the dynamic Hank's solution, more salt deposits are found. Fig. 8e shows that plentiful corrosion products are assembled in the manufacturing defect. Such a phenomenon is also found after the potentiodynamic polarization test (Fig. 3d). Nevertheless, there exist a significantly higher amount of corrosion products in the manufacturing defect of the 30-day immersed DT sample, specifying preferential sites for the salt deposition. Besides the general surface like that of ST sample (Fig. 8c), island-like surface is observed on the 30-day immersed DT sample (Fig. 8f). From EDS examinations at different locations, more salt deposits are detected at island-like features (Fig. 8f-G). The surface without the coverage of the island presents relatively low contents of Ca, P, and O (Fig. 8-f-F). Therefore, such islands are salt deposits. Fig. 8g shows scattered corrosion products on the surface of the 30-day immersed DT sample. Corrosion products are unevenly distributed. Higher contents of Ca, P, and O are detected at location H with more assembled corrosion products (Fig. 8f-H). Hodgson et al. [65] demonstrated that selective interactions of Ca^{2+} and PO_4^{3-} take

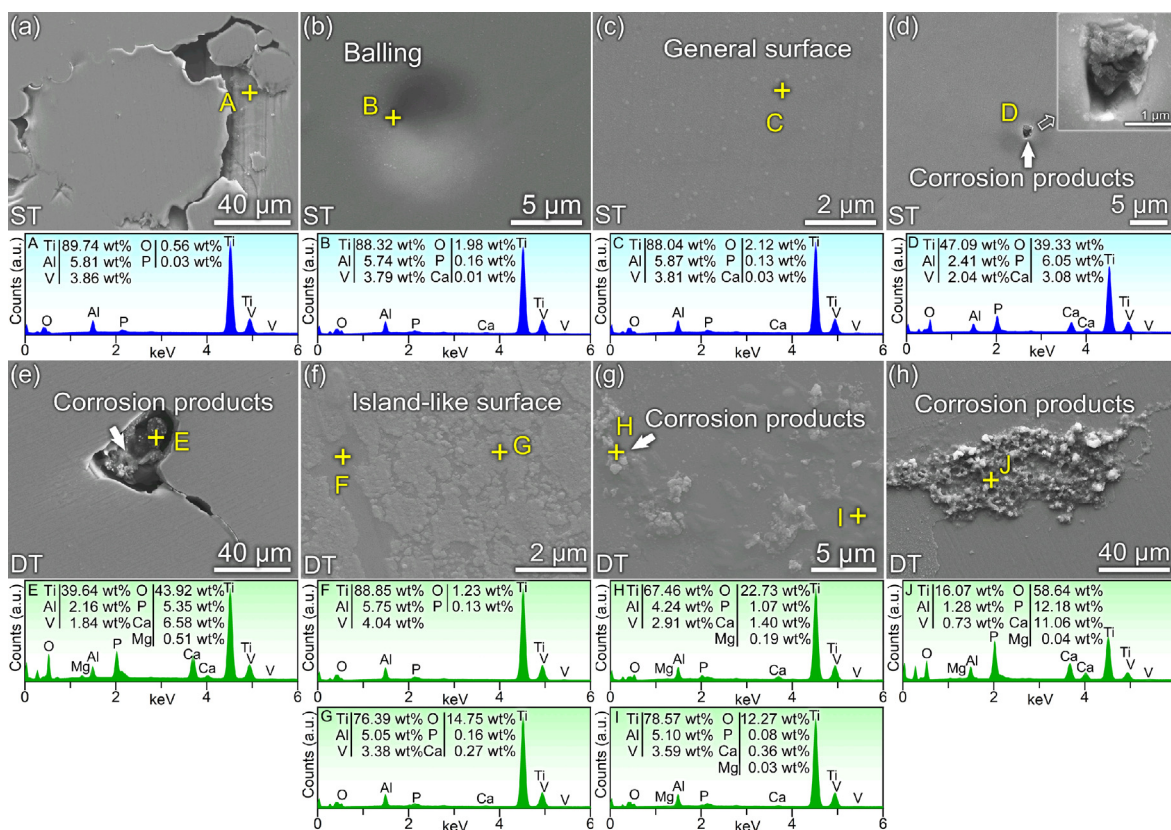Al ions on the passive film surface are prone to be ejected to the electrolyte [64].

Furthermore, salt deposition is more apparent on the surfaces of samples after 30-day immersion. Although the samples still have

Fig. 8. Secondary electron SEM images of surface morphologies of the Ti–6Al–4V samples after 30-day immersion tests: (a) manufacturing defect, (b) balling, (c) general surface and (d) corrosion product on the ST sample; (e) manufacturing defect, (f) island-like surface, (g) and (h) corrosion products on the surface of DT sample. The corresponding EDS spectra are below the SEM images. ST and DT indicate the selective laser melted Ti–6Al–4V tested in static and dynamic Hank's solutions at 37 °C, respectively.

place on the surface of passive films formed on Ti, Ti–6Al–4V, and Ti–6Al–7Nb in simulated body fluid. Therefore, the surface of the passive film would be remodeled after exposure. Fig. 8h represents the assembled corrosion products with relatively large sizes on the surface of the 30-day immersed DT sample. Only 16.07 wt% Ti is detected at location J (Fig. 8h-J). Therefore, it can be speculated that such assembled corrosion products have relatively higher thickness than those found in other locations, including those on the surface of the ST sample. Such assembled corrosion products are also rarely found on the surface of the 30-day immersed DT sample. In comparison, such assembled corrosion products are hardly found on the surface of the 30-day immersed ST sample during dedicated SEM examinations. Combining with the results in Fig. 3, several outcomes with respect to salt deposition can be simply concluded: (i) dynamic Hank's solution accelerates salt deposition; (ii) salt deposits are unevenly distributed; (iii) manufacturing defects are preferential sites for salt deposition; (iv) the amount of salt deposit increases with increasing the immersed time.

3.4.2. XPS analysis of passive films

Fig. 9 shows the depth profile of Ti, Al, V, Ca, P and O in the passive films obtained by XPS. A large fraction of O (77.7 at% for ST versus 82.5 at% for DT) and a certain fraction of Ca and P (Ca: 3.0 at% for ST versus 3.3 at% for DT; P: 1.7 at% for ST versus 2.7 at% for DT) are found at the surface of immersed samples. Such a high fraction of O is influenced by salt deposits on the surface of samples, which is attributed to the calcium phosphates [55]. The higher volume fractions of P and Ca also illustrate the higher amount of salt deposits on the surface of DT, which is consistent

with the outcome in Fig. 8. At the depth of 2 nm, the fraction of O rapidly decreases with the increase in the fraction of Ti. However, P is not detected at the depth of 2 nm for ST, while only 0.9 at% P is detected for DT. At the depth of 4 nm, P is neither detected for DT. Therefore, one can conclude that the average thicknesses of salt deposits are less than 2 nm for ST and less than 4 nm for DT after 30-day immersion. Although some salt deposits seem to be thicker than 4 nm in Fig. 8, it should be noted that the XPS spot is about 500 μm in diameter in this work and the obtained data is the summation of the detected area. The changes in the fractions of O and Ti become mild from the depth of 2 nm to 10 nm. With increasing the depth, the fractions of Ti and Al increase with the decline in the fraction of O, indicating that the growth of passive film formed on ST follows Fick's law [66,67]. As well known, the main components in the passive film formed on Ti alloys are Ti oxides, namely, TiO_2, Ti_2O_3, and TiO. In contrast, the DT always has a slightly higher fraction of O compared to the ST at the same depth of the passive film, specifying the easier ingression of O in the passive film formed on DT. Furthermore, V is almost undetected in the measured depth of passive film formed on both samples.

To clarify the corrosion products, Ti 2p, O 1s, Ca 2p and P 2p spectra obtained from the surfaces of the immersed ST and DT samples were analyzed, and the results are shown in Fig. 10. At the outer surface, Ti^{4+} state is revealed for both samples. Other states of Ti are not found. Such a result indicates that the passive films formed on the sample surfaces essentially consist of TiO_2. Nevertheless, hydroxyl groups are often found on the surfaces of corroded Ti and Ti alloys, in the form of titanium hydroxide and hydroxyapatite (HA, $Ca_{10}(PO_4)_6(OH)_2$, one of the salt deposits) [49,55]. Therefore, O 1s spectra were analyzed and deconvolved
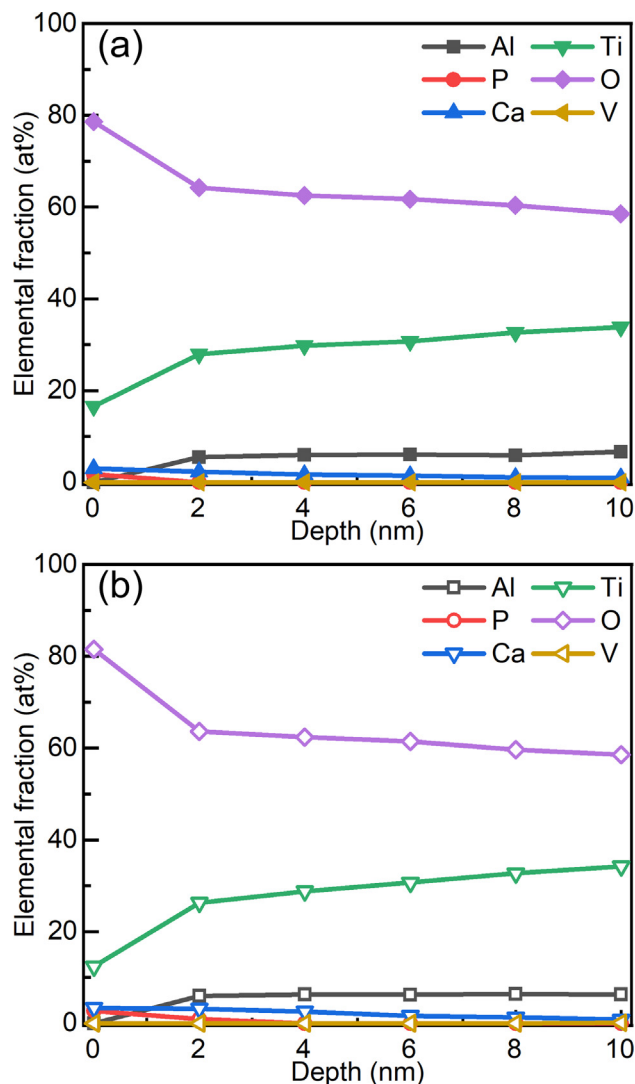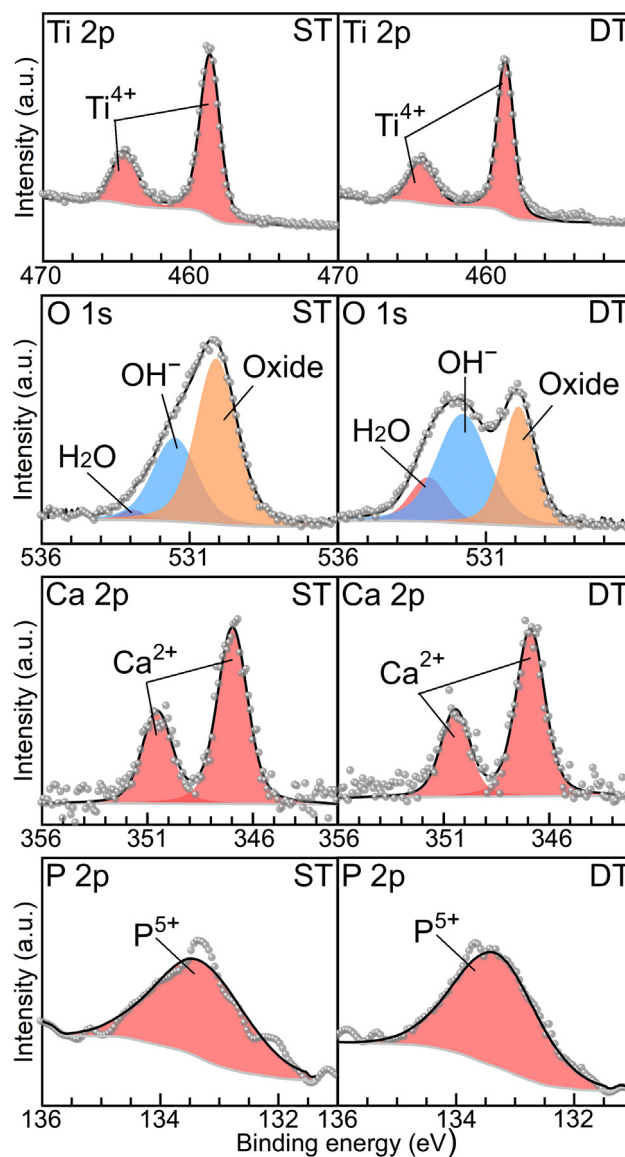
Fig. 9. Elemental fractions obtained from XPS results at different depths in the passive films formed on (a) ST and (b) DT. ST and DT indicate the selective laser melted Ti–6Al–4V tested in static and dynamic Hank's solutions at 37 °C, respectively.

Fig. 10. Ti 2p, O 1s, Ca 2p and P 2p spectra for ST and DT samples after 30-day immersion in the static and dynamic Hank's solutions at 37 °C. ST and DT indicate the selective laser melted Ti–6Al–4V tested in static and dynamic Hank's solutions at 37 °C, respectively.

into three components, which originate from oxide, hydroxyl groups, and water. For the ST sample, the fractions of oxide, hydroxyl groups, and water are 62.9 at%, 34.6 at%, and 2.5 at%, respectively. In comparison, the fractions of oxide, hydroxyl groups, and water are 35.2 at%, 50.3 at%, and 14.5 at%%, respectively for the DT sample. As shown in Fig. 8 and reported in Ref. [55], the salt deposits are discontinuous. Hence, both oxides and hydroxyl groups are detected within the spot of the XPS test. Oxide indicates the TiO_2 in the passive film, and hydroxyl groups play an important role in adsorbing phosphate ions to form HA. A larger fraction of hydroxyl groups detected on the surface of DT indicates the production of a larger amount of HA. Because the surface of the immersed sample is covered by salt deposits, the uncovered regions would be detected as oxides and hence high fraction of oxide is found for the immersed ST sample. Ca 2p and P 2p spectra confirm the existence of Ca^{2+} and P^{5+}. Such two ions mainly exist in the apatite and HA [49,55]. Combining with the results in Fig. 9, one can confirm that the salt deposits on both samples main consist of apatite and HA and DT shows more salt deposits.

Since the passive films formed on Ti–6Al–4V are predominantly composed of Ti oxides (TiO_2, Ti_2O_3, and TiO), the Ti 2p spectra

obtained at different depths of passive films are analyzed to investigate the ingression of O. Fig. 11 shows the deconvolution of Ti 2p spectra obtained at the depths of 2 nm, 6 nm, and 10 nm. As the sputtering depth increases, the peaks in XPS spectra generally shift to the region with lower binding energy. This finding indicates the decrease in the valence of Ti ion. The ratios of Ti oxides in the passive films can be quantitively obtained after deconvolution, as listed in Table 3. At the depth of 2 nm, the spectra of Ti 2p1/2 and Ti 2p3/2 are respectively deconvolved into three components, corresponding to Ti^{4+}, Ti^{3+}, and Ti^{2+} [34]. For ST, Ti^{4+}, Ti^{3+} and Ti^{2+} are 44.2 at%, 32.0 at% and 23.8 at%, respectively. By contrast, for DT, the corresponding ratios for Ti^{4+}, Ti^{3+} and Ti^{2+} are 53.6 at%, 35.8 at% and 10.6 at%, respectively. Hence, multi-step oxidation takes place for the formation of passive films on both samples. The passive film on DT has a relatively higher ratio of Ti^{4+} than that on ST. A similar scenario is also found at the other depths of passive films; the passive film formed on DT always has a higher ratio of highly charged Ti ions than that on ST at the same depth. As the
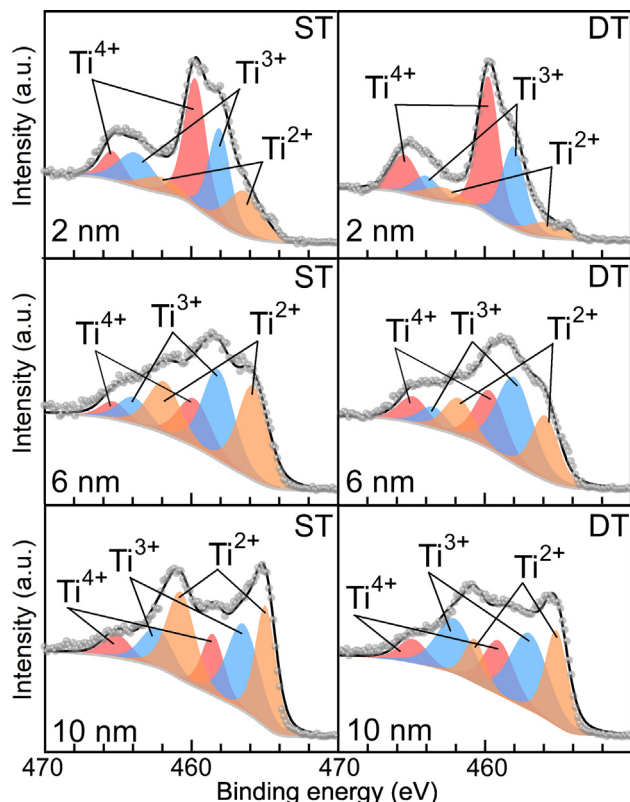
Fig. 11. Deconvolution of Ti 2p spectra at the depth of 2 nm, 6 nm and 10 nm for ST and DT samples after 30-day immersion in the static and dynamic Hank's solutions at 37 °C. ST and DT indicate the selective laser melted Ti–6Al–4V tested in static and dynamic Hank's solutions at 37 °C, respectively.

Fig. 12. Electrochemical impedance spectra of ST and DT samples after 30-day immersion: (a) Nyquist diagram and (b) Bode diagram. ST and DT indicate the selective laser melted Ti–6Al–4V tested in static and dynamic Hank's solutions at 37 °C, respectively.

sputtering depth increases, the fraction of Ti^{4+} gradually decreases and the fraction of Ti^{2+} gradually increases for both samples. As known, the oxygen content always gradually decreases with increasing the depth of passive film formed on the passive metals [34,66]. Such a finding illustrates that the passive film formed on Ti–6Al–4V would be thicker in dynamic Hank's solution than in static Hank's solution. This is well consistent with the Mott-Schottky measurement after potentiostatic polarization (Fig. 6).
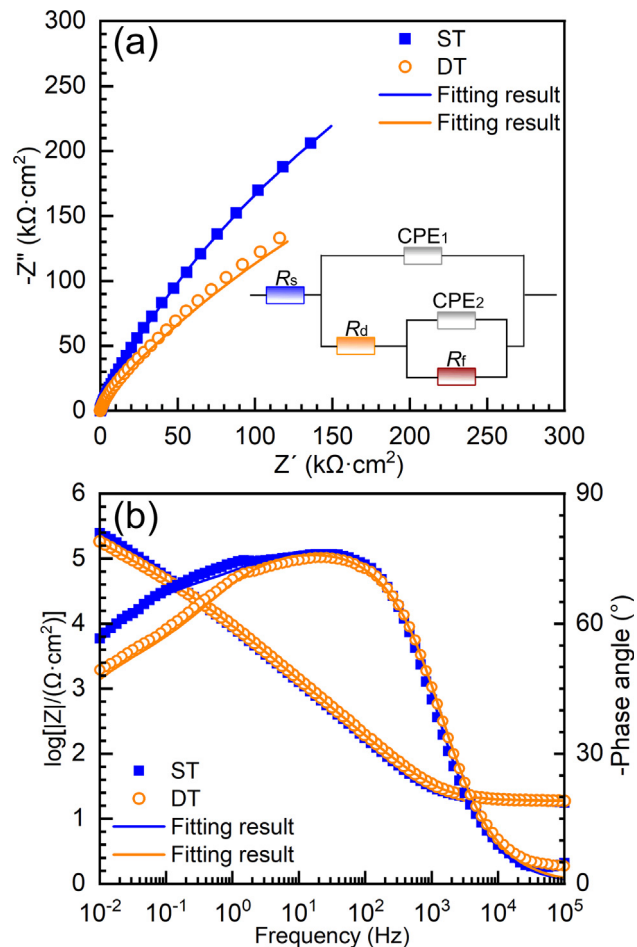
3.4.3. Electrochemical impedance spectra of immersed samples

Fig. 12 shows the electrochemical impedance spectra of immersed samples. In comparison to the results presented in Fig. 2, the differences in the passive films formed on ST and DT samples become more apparent, indicating distinct corrosion behavior of L-PBF-produced Ti–6Al–4V samples in dynamic Hank's

Table 3
Ratios of different valence Ti ions in the passive films formed on the laser powder bed fusion produced Ti–6Al–4V alloy at different depths after 30-day immersion in the static (ST) and dynamic (DT) Hank's solutions at 37 °C.

Depth	Samples	Ti^{4+} (at%)	Ti^{3+} (at%)	Ti^{2+} (at%)
2 nm	ST	44.2	32.0	23.8
	DT	53.6	35.8	10.6
4 nm	ST	27.3	42.8	29.9
	DT	31.6	51.7	16.7
6 nm	ST	22.0	39.2	38.8
	DT	27.3	46.7	26.0
8 nm	ST	19.7	40.4	39.9
	DT	25.6	44.3	30.1
10 nm	ST	19.5	40.8	39.7
	DT	24.6	43.2	32.2

solution in a long term. Considering the salt deposits, an alternative of $R(Q(R(QR)))$ is used to fit the EIS data obtained from the samples after 30-day immersion. The fitted results from Fig. 12 are listed in Table 4. The significantly low χ^2 illustrates the good quality of fitting. R_d means the resistance of salt deposits and R_f indicates the resistance of the passive film. Other symbols have the same meaning as the corresponding ones described in Section 3.2. As indicated in Sections 3.4.1 and 3.4.2, DT exhibits a larger quantity of salt deposits. Therefore, ST has a significantly lower R_d (24.03 ± 3.70 kΩ·cm²) than DT (37.49 ± 2.10 kΩ·cm²). Both samples demonstrate larger R_{ct} values by one order of magnitude than their corresponding R_d. Hence, R_{ct} basically determines the corrosion resistance of both immersed samples. After 30-day immersion, ST still shows a higher R_{ct} (1.44 ± 0.03 MΩ·cm²) than DT (1.07 ± 0.37 MΩ·cm²), which is similar to the results after OCP test. Therefore, one can find that the dynamic Hank's solution degrades the corrosion resistance of L-PBF-produced Ti–6Al–4V samples.

4. Discussion

4.1. Influence of dynamic Hank's solution on the corrosion behavior and salt deposition

In this work, the corrosion behavior of experimental targets is respectively investigated based on the L-PBF-produced alloy samples and 30-day immersed samples in both static and dynamic

Table 4
Fitting results of electrochemical impedance spectra of the laser powder bed fusion produced Ti–6Al–4V alloy after 30-day immersion in the static (ST) and dynamic (DT) Hank's solutions at 37 °C. R_s means solution resistance, R_d means film resistance, R_{ct} indicates charge transfer resistance, CPE describes charge transfer capacitance, n_1 and n_2 are the exponents of CPE_1 and CPE_2, χ^2 is the sum of squares of the differences between theoretical and experimental points.

Sample	R_s ($\Omega \cdot cm^2$)	R_d ($k\Omega \cdot cm^2$)	$CPE_1 \times 10^{-5}$ ($F \cdot cm^{-2}$)	n_1	R_{ct} ($M\Omega \cdot cm^2$)	$CPE_2 \times 10^{-5}$ ($F \cdot cm^{-2}$)	n_2	χ^2
ST	18.69 ± 0.64	24.03 ± 3.70	1.99 ± 0.09	0.8843 ± 0.0060	1.44 ± 0.03	1.00 ± 0.04	0.5947 ± 0.0097	6.62×10^{-4}
DT	18.92 ± 0.10	37.49 ± 2.10	1.98 ± 0.01	0.8694 ± 0.0009	1.07 ± 0.37	1.84 ± 0.02	0.5414 ± 0.0069	9.39×10^{-4}

Hank's solution, which can be regarded as short-term corrosion and long-term corrosion. L-PBF-produced Ti–6Al–4V alloy displays a typical passivation phenomenon in Hank's solution due to the high chemical activity of Ti [53]. However, passive films formed on L-PBF-produced Ti–6Al–4V alloy in a dynamic Hank's solution demonstrate lower protectiveness despite a relatively low flow rate. For instance, a thin passive film would be spontaneously formed during the OCP measurement which can be considered as 30-min corrosion in Hank's solution. The subsequent EIS measurement shows that the DT sample has a lower R_{ct} compared with the ST counterpart (Table 2). Since the value of R_{ct} indicates the resistance of the electrode process, the lower R_{ct} of the passive film formed on the DT sample elucidates its lower protectiveness. A similar scenario is found the Ref. [27]. The EIS results also show that the 30-days immersed samples have lower R_{ct} (Table 4). Nesic et al. [68] pointed out that the passive films on metals can be locally or globally thinned in a dynamic electrolyte. This outcome is further confirmed by the results of potentiostatic polarization (Fig. 4). The quasi-steady-state current densities for DT are approximately 1.5 times larger than those for ST at varied applied potentials. Generally, quasi-steady state current can be considered as the ratio of applied potential and impedance of passive film. Regardless of the instinct characteristics, passive films with lower thicknesses generally have lower impedance when formed under the same condition [34]. Therefore, higher quasi-steady-state current density often corresponds to lower thickness of passive films under a specific condition (as indicated by the function of film thickness and applied potentials, Figs. 4, and 6b). However, the passive films formed on DT with larger thicknesses exhibit higher quasi-steady-state current densities compared with those formed on ST at the same applied potential. Therefore, one may conclude that the quality of passive films formed on DT is not as good as that on ST. Similar results are also obtained from the 30-day immersed samples, by EIS examinations. One should note that the quasi-steady state current density (including the passivation current density) is a result of ion migration in the passive film formed on metals, which is determined by both the concentration diffusion gradient (J_C) and potential gradient (J_P) of oxygen vacancy [38]. J_P is proportional to the product D_o and N_D [34]. In this work, the DT sample have a higher D_o and N_D than the ST sample under each applied potential (Fig. 6a and c). Hence, the DT sample undoubtedly has a higher J_P. According to the results in Fig. 6a and c, the J_P of DT sample is about two times larger than that of ST sample under each potential. Furthermore, it is known than the oxygen vacancy is closed to Ti^{3+} and Ti^{2+} in passive film [69]. Hence, J_C can be assessed by the fraction of Ti^{3+} and Ti^{2+} at different depth. As seen from Fig. 10, only Ti^{4+} is detected on the surfaces of ST and DT samples. Meanwhile, the fractions of Ti^{3+} and Ti^{2+} are 40.8 at% and 39.7 at% for the ST sample and 43.2 at% and 32.2 at%, respectively (Table 3). Based on the electroneutrality principle [70], Ti^{3+} and Ti^{2+} may produce (or stabilize) one and two oxygen vacancies in a location. Therefore, it can be understood that the difference in the J_C of ST and DT sample is not apparent. As such, J_P is dominant in the ion migration of passive film and the DT sample has higher the quasi-steady state current density in the potentiostatic polarization test and the passivation current density in the potentiodynamic polarization test. Such results indicate that the flowing electrolyte would

reduce the corrosion resistance of L-PBF-produced Ti–6Al–4V (Figs. 2 and 4).

The passive films formed on both samples exhibit close chemical compositions as well as phase constituents, indicating that both ST and DT samples have a similar electrochemical process during corrosion (Figs. 9–11). However, the mass transfer on the surface of samples seems to be different. The electrolyte has a definite solubility for ions at specific pH and temperature [71]. Therefore, the dissolving ions can easily approach the solubility of the solution in the vicinity of the film surface in static Hank's solution, which reduces the concentration gradient of metal ions at the film/solution interface and therefore the dissolution rate of passive films. Kain et al. [71] reported that the flowing electrolyte would take away a large number of dissolved metal ions and supply the ions consumed in the solution. Hence, a high dissolution rate of metal ions maintains. As a result, more metal ions are released from L-PBF-produced Ti–6Al–4V in dynamic Hank's solution (Fig. 7). On the other hand, the high dissolution rate of metal ions increases their concentration gradients in the passive film, resulting in the continuous transformation of metallic atoms to metallic ions and electron-vacancy pairs (oxygen vacancy) [47]. As such, the higher density of oxygen vacancy and higher vacancy diffusion coefficient are achieved for the DT sample (Fig. 6a and 6c). Such results are consistent with the outcomes mentioned in the previous paragraph. In the dynamic solution, the consumed ions can be supplied on the surface of sample [71]. Therefore, the higher concentration of O^{2-} on the surface of the DT sample and higher vacancy diffusion coefficient in the passive film corporately contribute to a higher growth rate of passive film (Fig. 6).

Furthermore, it was reported that the formation of apatite in Hank's solution results from the reaction between PO_4^{4-} and Ca^{2+} [55]. The surface of the passive film formed on Ti and Ti alloys is generally negative-charged at pH = 7.4 in simulated body fluid due to the absorption of OH^- [72]. Hence, positive-charged ions, such as Ca^{2+} and H^+, would be electrostatically attracted. Meanwhile, the passive films are still capable of adsorbing species with negative charges; exchange reaction with phosphate groups to form Ti-phosphates can take place on the hydrated surface of passive films, which further produces apatite by reacting with adsorbed Ca^{2+} [72]. Both Ca^{2+} and PO_4^{4-} come from Hank's solution. The DT samples have more salt deposits on their surfaces (Figs. 3 and 8–10). Such a finding also can be attributed to the supplement of new Ca^{2+} and PO_4^{4-} from fresh solution provided by flowing Hank's solution. Siriphannon et al. [73] found that more apatite can be formed on the sample in the flowing simulated body fluid at a relatively low rate. In this work, the flow rate of Hank's solution is also low, which is in line with the result in Ref. [73]. Another phenomenon, "flow mark", was observed by Xu et al. [45] on corroded X65 pipeline steel due to the high shear stress on the surface sample (produced by flowing electrolyte in a high rate). However, no such "flow marks" are observed on the surface of the DT sample, which is also attributed to the relatively low flowing rate of electrolyte in this work. However, there is still evidence that the dynamic Hank's solution has a mechanical effect on the passive films. As seen in Fig. 8, calcium phosphates are prone to be deposited in the pores. Notably, the amount of calcium phosphate is relatively low at the other locations (besides the large-sized corrosion

products). Therefore, it is speculated that the adsorbed ions or exchanged ions may be taken away by the flow solution. Relatively, such a mechanical effect would not be apparent in the pores. Therefore, pores become the preferential sites for salt deposition. Unlike other Ti parts produced by some conventional technologies, pores are unavoidable in the L-PBF-produced Ti parts. Therefore, the salt deposition phenomenon of L-PBF-produced Ti parts would be more apparent, especially in the dynamic Hank's solution. Based on the above discussion, one can understand that the corrosion resistance of Ti–6Al–4V is reduced in the dynamic Hank's solution and the lifetime of this alloy may be not expected as in static Hank's solution.

4.2. Formation of passive film in the dynamic Hank's solution

It is well known that the growth of passive film is determined by the diffusion of oxygen vacancies and metal vacancies between the film/solution and metal/film interfaces [34]. In terms of the point defect model (PDM) [47], the passive film formed on L-PBF-produced Ti–6Al–4V can be rationalized as schematically shown in Fig. 13. In Fig. 13, defects are denoted according to Kröger–Vink notation [74]; Ti_{Ti} and Al'_{Ti} are Ti and Al ions in the cation sites of passive film, $V^{..}_{o}$ and $V^{4'}_{Ti}$ are oxygen vacancy and Ti ion vacancy in the passive film, V_{Ti} is vacancy in the substrate, e' is an electron, O_o is oxygen ion in anion site of the passive film, $Ti^{4+}_{(aq)}$ and $Al^{3+}_{(aq)}$ are Ti and Al ions in solution. During the corrosion of Ti and Ti alloys in the aqueous solution, five reactions primarily take place in the following sequence. (i) Ti (or Al) atoms enter the passive film and become Ti_{Ti} (or Al'_{Ti}); meanwhile, $V^{..}_{o}$ are produced due to the incomplete oxidation of metallic ions (local electroneutrality [63]). (ii) Ti (or Al) atoms enter passive film by exchanging with $V^{4'}_{Ti}$ and produce Ti_{Ti} (or Al'_{Ti}) in the passive film. Such two reactions take place at the metal/film interface. (iii) Ti_{Ti} or Al'_{Ti} on the surface of the passive film may be ejected and becomes $Ti^{4+}_{(aq)}$ and $Al^{3+}_{(aq)}$ due to their thermal motion; meanwhile, $V^{4'}_{Ti}$ is produced at the original positions of Ti_{Ti} or Al'_{Ti}. (iv) The produced $V^{..}_{o}$ migrates to the film/-solution interface and reacts with H_2O to produce H^+ and O_o. (v) TiO_2 and Al_2O_3 on the surface of passive films react with the H^+ in the solution and produce $Ti^{4+}_{(aq)}$, $Al^{3+}_{(aq)}$ and H_2O. Notably, reactions (ii), (iii) and (iv) involve the movement of ions across the boundaries and hence conserve the passive film. Reaction (i) indicates the formation of new passive film and reaction (v) illustrates the dissolution of passive film. Such a process for the formation of passive films on the Ti and Ti alloys have also been reported in Refs. [47,75].

Actually, the formation mechanism of passive films in the static and dynamic Hank's solution would be identical. However, as mentioned above, dynamic Hank's solution accelerates the mass transfer on the surface of the passive film. Since the migration of oxygen vacancies is significantly faster than that of metal vacancies, a considerable number of metal vacancies are accumulated at the surface of the passive film (Fig. 6c). Therefore, the surface of the passive film formed on metals is generally negative-charged [38]. In this situation, H^+ in the solution would be captured, resulting in the dissolution of the passive film due to the reaction (v). As mentioned above, the DT sample has a higher fraction of Ti^{4+} in the vicinity of the film surface (Table 3). Therefore, $V^{4'}_{Ti}$ is prone to be produced at the surface of the passive film (reaction (iii)). The produced $V^{4'}_{Ti}$, in turn, promotes the capture of H^+. Therefore, the dissolution of passive film is accelerated in the dynamic Hank's solution. In the meantime, the consumption of H^+ also activates the reaction (iv). Therefore, $V^{..}_{o}$ on the surface of passive film is easier to be consumed in the dynamic Hank's solution, which may also result in a higher concentration gradient of $V^{..}_{o}$ between metal/film and film/solution interfaces and promote the transformation of metallic atoms to ions and oxygen vacancy (reaction (i)). In addition, Al^{3+} is less charged than Ti^{4+} in the passive film. Oxygen vacancy is inevitably generated to keep the local electroneutrality in the passive film [63]. Therefore, the higher Al ion release (Fig. 7) also indicates the continuous transformation of metallic Al to ionic Al and electron-vacancy pairs at the metal/film interface (reaction
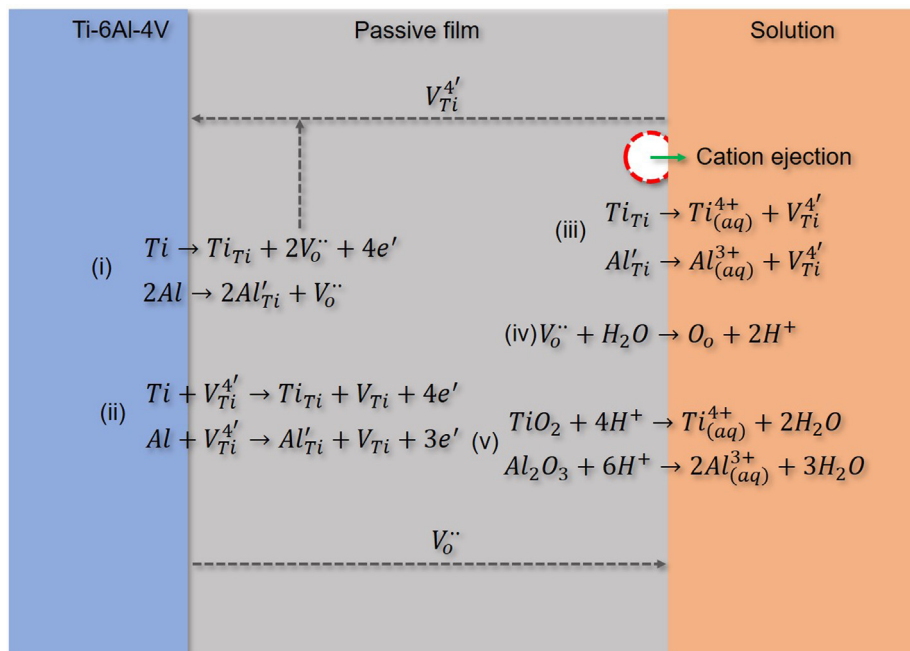
Fig. 13. Schematic illustration of the formation and dissolution of passive film formed on selective laser melted Ti–6Al–4V4V alloy in Hank's solution in terms of point defect model. Ti_{Ti} and Al'_{Ti} are Ti and Al ions in cation sites of passive film, $V^{..}_{o}$ and V^{4}_{Ti} are oxygen vacancy and Ti ion vacancy in passive film, V_{Ti} is vacancy in Ti–6Al–4V substrate, e' is an electron, O_o is oxygen ion in anion site of passive film, $Ti^{4+}_{(aq)}$ and $Al^{3+}_{(aq)}$ are Ti ion and Al ion in solution.

(i)). Such a result, in turn, increases the concentration gradient of $V_o^{..}$ therefore the oxygen diffusion coefficient in the passive film. As a result, DT samples have higher oxygen diffusion coefficient at various applied potentials (Fig. 6c). Hence, the growth rate of passive film is facilitated in the dynamic Hank's solution. The entire corrosion process of the sample is accelerated by dynamic Hank's solution, resulting in higher growth rate, higher density of donor and higher oxygen diffusion coefficient of passive film as well as higher ion release (Figs. 6 and 7).

5. Conclusions

In this work, the corrosion behavior of laser powder bed fusion produced (L-PBF-produced) Ti–6Al–4V alloy in both static (ST) and dynamic (DT) Hank's solutions at 37 °C was investigated based on the as L-PBF-produced alloy samples and 30-day immersed samples. The characteristics of formed passive films were examined by electrochemical measurement, scanning electron microscopy, and X-ray photoelectron spectroscopy (XPS) to disclose the underlying mechanism. Some key conclusions can be drawn as follows:

1. ST and DT samples show similar potentiodynamic polarization behavior. However, ST has a slightly lower passive current density (6.355 ± 0.167 $\mu A \cdot cm^{-2}$) than DT (6.683 ± 0.526 $\mu A \cdot cm^{-2}$). Electrochemical impedance spectroscopy (EIS) results show that the passive films formed on DT after immersion for 1800 s have a lower charge transfer (0.689 ± 0.11 $M\Omega \cdot cm^2$) impedance compared with those on ST (0.774 ± 0.15 $M\Omega \cdot cm^2$).

2. The passive films, which were respectively prepared by potentiostatic polarization ranging from 0.6 V_{SCE} to 1.0 V_{SCE}, formed on both samples show typical *n*-type semiconductor properties. The calculated density of donors for DT is higher than those for ST at varied potentials. Meanwhile, the calculated diffusion coefficients of oxygen vacancy and film thickness for DT are also higher than those for ST, indicating that passive film has a faster growth rate in the dynamic Hank's solution.

3. 30-day immersion tests were conducted to examine the long-term corrosion behavior of both samples. XPS results indicate that the passive films formed on both immersed ST and DT samples mainly consist of TiO_2, Ti_2O_3, and TiO. The passive film formed on DT has a higher oxygen concentration than that formed on ST at the same depth. Meanwhile, DT has a higher ion release (e.g. Ti^{4+} and Al^{3+}) than ST after 30-day immersion. Both findings illustrate a higher rate of formation and dissolution of passive film formed on DT.

4. Salt deposition, which mainly results from the calcium and phosphate ions in Hank's solution, takes place for ST and DT samples both after the potentiodynamic polarization test and the 30-day immersion test. The salt deposits on both samples main consist of apatite and hydroxyapatite. The dynamic Hank's solution accelerates the salt deposition and the amount of salt deposit increases with increasing the immersed time. Meanwhile, manufacturing defects on the surface of the sample are preferential sites for salt deposition.

5. The distinct corrosion behavior of L-PBF-produced Ti–6Al–4V alloy as well as their different characteristics of passive films are mainly attributed to the mass-transfer effect of dynamic Hank's solution. Dynamic Hank's solution provides more calcium and phosphate ions to the surface of the passive film, resulting in more salt deposits. In terms of point defect model, dynamic Hank's solution results in a higher dissolution rate of metal ions and therefore the continuous transformation of metallic Ti to ionic Ti and oxygen vacancy, leading to a higher density of oxygen vacancy and a higher oxygen diffusion coefficient of the passive film formed on the DT sample.

6. Data availability

The raw/processed data required to reproduce these findings cannot be shared at this time as the data also forms part of an ongoing study.

Declaration of Competing Interest

The authors declare that they have no known competing financial interests or personal relationships that could have appeared to influence the work reported in this paper.

References

[1] T. DebRoy, H. Wei, J. Zuback, T. Mukherjee, J.W. Elmer, J.O. Milewski, A.M. Beese, A. Wilson-Heid, A. De, W. Zhang, Additive manufacturing of metallic components–process, structure and properties, Prog. Mater. Sci. 92 (2018) 112–224.

[2] C.A. Biffi, P. Bassani, J. Fiocchi, M. Albu, A. Tuissi, Selective laser melting of AlCu-TiB2 alloy using pulsed wave laser emission mode: processability, microstructure and mechanical properties, Mater. Des. 204 (2021) 109628.

[3] L.Y. Wang, Y.C. Wang, Z.J. Zhou, H.Y. Wan, C.P. Li, G.F. Chen, G.P. Zhang, Small punch creep performance of heterogeneous microstructure dominated Inconel 718 fabricated by selective laser melting, Mater. Des. 195 (2020) 109042.

[4] D. Gu, J. Yang, K. Lin, C. Ma, L. Yuan, H. Zhang, M. Guo, H. Zhang, Compression performance and mechanism of superimposed sine-wave structures fabricated by selective laser melting, Mater. Des. 198 (2021) 109291.

[5] E.O. Olakanmi, R.F. Cochrane, K.W. Dalgarno, A review on selective laser sintering/melting (SLS/SLM) of aluminium alloy powders: Processing, microstructure, and properties, Prog. Mater. Sci. 74 (2015) 401–477.

[6] L.-C. Zhang, H. Attar, Selective Laser Melting of Titanium Alloys and Titanium Matrix Composites for Biomedical Applications: A Review Adv, Eng. Mater. 18 (2016) 463–475.

[7] L.-C. Zhang, H. Attar, M. Calin, J. Eckert, Review on manufacture by selective laser melting and properties of titanium based materials for biomedical applications, Mater. Tech. 31 (2016) 66–76.

[8] Y.J. Liu, Y.S. Zhang, L.C. Zhang, Transformation-induced plasticity and high strength in beta titanium alloy manufactured by selective laser melting, Materialia 6 (2019) 100299.

[9] L.C. Zhang, D. Klemm, J. Eckert, Y.L. Hao, T.B. Sercombe, Manufacture by selective laser melting and mechanical behavior of a biomedical Ti-24Nb-4Zr-8Sn alloy, Scripta Mater. 65 (2011) 21–24.

[10] S.J. Li, T.C. Cui, Y.L. Hao, R. Yang, Fatigue properties of a metastable β-type titanium alloy with reversible phase transformation, Acta Biomater. 4 (2008) 305–317.

[11] B. Vrancken, L. Thijs, J.-P. Kruth, J. Van Humbeeck, Heat treatment of Ti6Al4V produced by Selective Laser Melting: Microstructure and mechanical properties, J. Alloys Compd. 541 (2012) 177–185.

[12] M. Niinomi, Mechanical properties of biomedical titanium alloys, Mater. Sci. Eng. A 243 (1998) 231–236.

[13] M. Geetha, A.K. Singh, R. Asokamani, A.K. Gogia, Ti based biomaterials, the ultimate choice for orthopaedic implants–a review, Prog. Mater. Sci. 54 (2009) 397–425.

[14] M. Qian, W. Xu, M. Brandt, H.P. Tang, Additive manufacturing and postprocessing of Ti-6Al-4V for superior mechanical properties, MRS Bull. 41 (2016) 775–784.

[15] S.L. Lu, H.P. Tang, Y.P. Ning, N. Liu, D.H. StJohn, M. Qian, Microstructure and mechanical properties of long Ti-6Al-4V rods additively manufactured by selective electron beam melting out of a deep powder bed and the effect of subsequent hot isostatic pressing, Metall. Mater. Trans. A 46 (2015) 3824–3834.

[16] N. Dai, L.-C. Zhang, J. Zhang, Q. Chen, M. Wu, Corrosion behavior of selective laser melted Ti-6Al-4V alloy in NaCl solution, Corros. Sci. 102 (2016) 484–489.

[17] J. Yang, H. Yang, H. Yu, Z. Wang, X.J.M. Zeng, Corrosion behavior of additive manufactured Ti-6Al-4V alloy in NaCl solution, Metall. Mater. Trans. A 48 (2017) 3583–3593.

[18] H. Zhang, C. Man, C. Dong, L. Wang, W. Li, D. Kong, L. Wang, X. Wang, The corrosion behavior of Ti6Al4V fabricated by selective laser melting in the artificial saliva with different fluoride concentrations and pH values, Corros. Sci. 179 (2021) 109097.

[19] H.M. Hamza, K.M. Deen, W. Haider, Microstructural examination and corrosion behavior of selective laser melted and conventionally manufactured Ti6Al4V for dental applications, Mater. Sci. Eng. C 113 (2020) 110980.

[20] D.-I. Seo, J.-B. Lee, Corrosion Characteristics of Additive-Manufactured Ti-6Al-4V Using Microdroplet Cell and Critical Pitting Temperature Techniques, J. Electrochem. Soc. 166 (2019) C428–C433.

[21] N. Dai, L.-C. Zhang, J. Zhang, X. Zhang, Q. Ni, Y. Chen, M. Wu, C. Yang, Distinction in corrosion resistance of selective laser melted Ti-6Al-4V alloy on different planes, Corros. Sci. 111 (2016) 703–710.

[22] B. Zhao, H. Wang, N. Qiao, C. Wang, M. Hu, Corrosion resistance characteristics of a Ti-6Al-4V alloy scaffold that is fabricated by electron beam melting and selective laser melting for implantation in vivo, Mater. Sci. Eng. C 70 (2017) 832–841.

[23] D. Kong, C. Dong, X. Ni, X. Li, Corrosion of metallic materials fabricated by selective laser melting, Npj Mater. Degrad. 3 (2019) 1–14.

[24] P. Qin, Y. Chen, Y.-J. Liu, J. Zhang, L.-Y. Chen, Y. Li, X. Zhang, C. Cao, H. Sun, L.-C. Zhang, Resemblance in corrosion behavior of selective laser melted and traditional monolithic β Ti-24Nb-4Zr-8Sn alloy, ACS Biomater. Sci. Eng. 5 (2019) 1141–1149.

[25] L. Zhou, T. Yuan, J. Tang, J. He, R. Li, Mechanical and corrosion behavior of titanium alloys additively manufactured by selective laser melting – A comparison between nearly β titanium, α titanium and α + β titanium, Opt. Laser Tech. 119 (2019) 105625.

[26] Y. Chen, J. Zhang, N. Dai, P. Qin, H. Attar, L.-C. Zhang, Corrosion behaviour of selective laser melted Ti-TiB biocomposite in simulated body fluid, Electrochim. Acta 232 (2017) 89–97.

[27] X. Chen, Q. Fu, Y. Jin, M. Li, R. Yang, X. Cui, M. Gong, In vitro studying corrosion behavior of porous titanium coating in dynamic electrolyte, Mater. Sci. Eng. C 70 (2017) 1071–1075.

[28] N. Mavros, T. Larimian, J. Esqivel, R.K. Gupta, R. Contieri, T. Borkar, Spark plasma sintering of low modulus titanium-niobium-tantalum-zirconium (TNTZ) alloy for biomedical applications, Mater. Des. 183 (2019) 108163.

[29] Y.P. Dong, J.C. Tang, D.W. Wang, N. Wang, Z.D. He, J. Li, D.P. Zhao, M. Yan, Additive manufacturing of pure Ti with superior mechanical performance, low cost, and biocompatibility for potential replacement of Ti-6Al-4V, Mater. Des. 196 (2020) 109142.

[30] J. Wu, Y. Liu, Q. Cao, T. Yu, J. Zhang, Q. Liu, X. Yang, Growth factors enhanced angiogenesis and osteogenesis on polydopamine coated titanium surface for bone regeneration, Mater. Des. 196 (2020) 109162.

[31] E. Yılmaz, A. Gökçe, F. Findik, H. Gulsoy, Metallurgical properties and biomimetic HA deposition performance of Ti-Nb PIM alloys, J. Alloys Compd. 746 (2018) 301–313.

[32] E. Yılmaz, A. Gökçe, F. Findik, H.O. Gulsoy, O. İyibilgin, Mechanical properties and electrochemical behavior of porous Ti-Nb biomaterials, J. Mech. Behav. Biomed. Mater. 87 (2018) 59–67.

[33] E. Yılmaz, B. Çakıroğlu, A. Gökçe, F. Findik, H.O. Gulsoy, N. Gulsoy, Ö. Mutlu, M. Özacar, Novel hydroxyapatite/graphene oxide/collagen bioactive composite coating on Ti16Nb alloys by electrodeposition, Mater. Sci. Eng. C 101 (2019) 292–305.

[34] X. Gai, Y. Bai, J. Li, S. Li, W. Hou, Y. Hao, X. Zhang, R. Yang, R.D.K. Misra, Electrochemical behaviour of passive film formed on the surface of Ti-6Al-4V alloys fabricated by electron beam melting, Corros. Sci. 145 (2018) 80–89.

[35] P. Qin, L.Y. Chen, C.H. Zhao, Y.J. Liu, C.D. Cao, H. Sun, L.C. Zhang, Corrosion behavior and mechanism of selective laser melted Ti35Nb alloy produced using pre-alloyed and mixed powder in Hank's solution, Corros. Sci. 189 (2021) 109609.

[36] J.L. Wang, R.L. Liu, T. Majumdar, S.A. Mantri, V.A. Ravi, R. Banerjee, N. Birbilis, A closer look at the in vitro electrochemical characterisation of titanium alloys for biomedical applications using in-situ methods, Acta Biomater. 54 (2017) 469–478.

[37] N. Kahraman, B. Gulenc, F. Findik, Corrosion and mechanical-microstructural aspects of dissimilar joints of Ti–6Al–4V and Al plates, Int. J. Impact Eng. 34 (2007) 1423–1432.

[38] L. Guan, Y. Li, G. Wang, Y. Zhang, L.-C. Zhang, pH dependent passivation behavior of niobium in acid fluoride-containing solutions, Electrochim. Acta 285 (2018) 172–184.

[39] W. Xu, E.W. Lui, A. Pateras, M. Qian, M. Brandt, In situ tailoring microstructure in additively manufactured Ti-6Al-4V for superior mechanical performance, Acta Mater. 125 (2017) 390–400.

[40] S. Liu, Y.C. Shin, Additive manufacturing of Ti6Al4V alloy: A review, Mater. Des. 164 (2019) 107552.

[41] W. Xu, M. Brandt, S. Sun, J. Elambasseril, Q. Liu, K. Latham, K. Xia, M. Qian, Additive manufacturing of strong and ductile Ti–6Al–4V by selective laser melting via in situ martensite decomposition, Acta Mater. 85 (2015) 74–84.

[42] H.-Y. Yang, Z. Wang, L.-Y. Chen, S.-L. Shu, F. Qiu, L.-C. Zhang, Interface formation and bonding control in high-volume-fraction (TiC+TiB2)/Al composites and their roles in enhancing properties, Compos. Part B 209 (2021) 108605.

[43] B.-X. Dong, Q. Li, Z.-F. Wang, T.-S. Liu, H.-Y. Yang, S.-L. Shu, L.-Y. Chen, F. Qiu, Q.-C. Jiang, L.-C. Zhang, Enhancing strength-ductility synergy and mechanisms of Al-based composites by size-tunable in-situ TiB2 particles with specific spatial distribution, Compos. Part B 217 (2021) 108912.

[44] Y. Bai, X. Gai, S. Li, L.-C. Zhang, Y. Liu, Y. Hao, X. Zhang, R. Yang, Y. Gao, Improved corrosion behaviour of electron beam melted Ti-6Al–4V alloy in phosphate buffered saline, Corros. Sci. 123 (2017) 289–296.

[45] Y. Xu, M.Y. Tan, Probing the initiation and propagation processes of flow accelerated corrosion and erosion corrosion under simulated turbulent flow conditions, Corros. Sci. 151 (2019) 163–174.

[46] S.Y. Choy, C.-N. Sun, K.F. Leong, J. Wei, Compressive properties of Ti-6Al-4V lattice structures fabricated by selective laser melting: Design, orientation and density, Addit. Manuf. 16 (2017) 213–224.

[47] J. Li, X. Lin, J. Wang, M. Zheng, P. Guo, Y. Zhang, Y. Ren, J. Liu, W. Huang, Effect of stress-relief annealing on anodic dissolution behaviour of additive manufactured Ti-6Al-4V via laser solid forming, Corros. Sci. 153 (2019) 314–326.

[48] N. Dai, J. Zhang, Y. Chen, L.-C. Zhang, Heat treatment degrading the corrosion resistance of selective laser melted Ti-6Al-4V alloy, J. Electrochem. Soc. 164 (2017) C428–C434.

[49] T. Hanawa, Metal ion release from metal implants, Mater. Sci. Eng. C 24 (2004) 745–752.

[50] T. Hanawa, M. Ota, Calcium phosphate naturally formed on titanium in electrolyte solution, Biomaterials 12 (1991) 767–774.

[51] X. Gong, Y. Li, Y. Nie, Z. Huang, F. Liu, L. Huang, L. Jiang, H. Mei, Corrosion behaviour of CoCrMo alloy fabricated by electron beam melting, Corros. Sci. 139 (2018) 68–75.

[52] W. Vanderlinde, Energy Dispersive X-ray Analysis, in: R.J. Ross (Ed.), Microelectronics Fialure Analysis Desk Reference, ASM International, Materials Park, the United States of America, 2011, pp. 549–560.

[53] X. Liu, P.K. Chu, C. Ding, Surface modification of titanium, titanium alloys, and related materials for biomedical applications, Mater. Sci. Eng., R 47 (2004) 49–121.

[54] J.-R. Chen, W.-T. Tsai, In situ corrosion monitoring of Ti–6Al–4V alloy in H2SO4/HCl mixed solution using electrochemical AFM, Electrochim. Acta 56 (2011) 1746–1751.

[55] T. Hanawa, M. Ota, Characterization of surface film formed on titanium in electrolyte using XPS, Appl. Surf. Sci. 55 (1992) 269–276.

[56] Q. Yan, H. Yoshioka, H. Habazaki, A. Kawashima, K. Asami, K. Hashimoto, The pitting corrosion behavior of sputter-deposited amorphous Al-Ti alloys in a neutral chloride-containing solution, J. Non-Cryst. Solids 125 (1990) 25–31.

[57] M. Lakatos-Varsányi, F. Falkenberg, I. Olefjord, The influence of phosphate on repassivation of 304 stainless steel in neutral chloride solution, Electrochim. Acta 43 (1998) 187–197.

[58] R.M. Fernández-Domene, E. Blasco-Tamarit, D.M. García-García, J. García-Antón, Passive and transpassive behaviour of Alloy 31 in a heavy brine LiBr solution, Electrochim. Acta 95 (2013) 1–11.

[59] F. Sun, G. Meng, T. Zhang, Y. Shao, F. Wang, C. Dong, X. Li, Electrochemical corrosion behavior of nickel coating with high density nano-scale twins (NT) in solution with Cl−, Electrochim. Acta 54 (2009) 1578–1583.

[60] L. Wang, H. Yu, S. Wang, B. Chen, Y. Wang, W. Fan, D. Sun, Quantitative analysis of local fine structure on diffusion of point defects in passive film on Ti, Electrochim. Acta 314 (2019) 161–172.

[61] H.-H. Huang, Effects of fluoride concentration and elastic tensile strain on the corrosion resistance of commercially pure titanium, Biomaterials 23 (2002) 59–63.

[62] R. Azadbakht, T. Almasi, H. Keypour, M. Rezaeivala, A new asymmetric Schiff base system as fluorescent chemosensor for Al3+ ion, Inorg. Chem. Commun. 33 (2013) 63–67.

[63] L. Chen, J. Li, Y. Zhang, LC. Zhang, W. Lu, L. Zhang, L. Wang, D. Zhang, Effects of alloyed Si on the autoclave corrosion performance and periodic corrosion kinetics in Zr-Sn-Nb-Fe-O alloys, Corros. Sci. 100 (2015) 651–662.

[64] M. Hashimoto, S. Miyajima, T. Murata, A spectrum analysis of potential fluctuation during passive film breakdown and repair on iron, Corros. Sci. 33 (1992) 917–925.

[65] A.W.E. Hodgson, Y. Mueller, D. Forster, S. Virtanen, Electrochemical characterisation of passive films on Ti alloys under simulated biological conditions, Electrochim. Acta 47 (2002) 1913–1923.

[66] L. Zhang, L.-Y. Chen, C. Zhao, Y. Liu, L.-C. Zhang, Calculation of oxygen diffusion coefficients in oxide films formed on low-temperature annealed Zr alloys and their related corrosion behavior, Metals 9 (2019) 850.

[67] Z. Jiang, X. Dai, T. Norby, H. Middleton, Investigation of pitting resistance of titanium based on a modified point defect model, Corros. Sci. 53 (2011) 815–821.

[68] S. Nešić, G.T. Solvi, J. Enerhaug, Comparison of the Rotating Cylinder and Pipe Flow Tests for Flow-Sensitive Carbon Dioxide Corrosion, Corrosion 51 (1995) 773–787.

[69] Y. Fang, Z. Liu, J. Han, Z. Jin, Y. Han, F. Wang, Y. Niu, Y. Wu, Y. Xu, High-Performance Electrocatalytic Conversion of N2 to NH3 Using Oxygen-Vacancy-Rich TiO2 In Situ Grown on Ti3C2Tx MXene, Adv. Energy Mater. 9 (2019) 1803406.

[70] L.P. Savtchenko, M.M. Poo, D.A. Rusakov, Electrodiffusion phenomena in neuroscience: a neglected companion, Nat. Rev. Neurosci. 18 (2017) 598.

[71] V. Kain, Flow accelerated corrosion: forms, mechanisms and case studies, Proc. Eng. 86 (2014) 576–588.

[72] J. Pan, D. Thierry, C. Leygraf, Electrochemical and XPS studies of titanium for biomaterial applications with respect to the effect of hydrogen peroxide, J. Biomed. Mater. Res. 28 (1994) 113–122.

[73] P. Siriphannon, Y. Kameshima, A. Yasumori, K. Okada, S. Hayashi, Comparitive study of the formation of hydroxyapatite in simulated body fluid under static and flowing systems, J. Biomed. Mater. Res. 60 (2002) 175–185.

[74] Y. Dong, L. Qi, J. Li, I.W. Chen, A computational study of yttria-stabilized zirconia: II. Cation diffusion, Acta Mater. 126 (2017) 438–450.

[75] P. Bocchetta, L.-Y. Chen, J.D. Tardelli, A.C. Reis, F. Almeraya-Calderón, P. Leo, Passive Layers and Corrosion Resistance of Biomedical Ti-6Al-4V and β-Ti Alloys, Coatings 11 (2021).